Direct Numerical Simulations of premixed methane flame initiation by pilot n-heptane spray autoignition

E. Demosthenous[1,*], G. Borghesi[2], E. Mastorakos[1], R. S. Cant[1]

* Corresponding author. Email address: ed398@cam.ac.uk

1: Department of Engineering, University of Cambridge

Trumpington Street, Cambridge CB2 1PZ, UK

Tel: +44 1223 332641

Fax: +44 1223 339906

2: Jet Propulsion Laboratory, California Institute of Technology

4800 Oak Grove Drive, MS 125-130 Pasadena, CA 91109-8099, USA

Direct Numerical Simulations of premixed methane flame initiation by pilot n-heptane spray autoignition

E. Demosthenous, G. Borghesi, E. Mastorakos, R. S. Cant

Hopkinson Laboratory, Department of Engineering, University of Cambridge, Cambridge CB2 1PZ, UK

Abstract

Autoignition of n-heptane sprays in a methane/air mixture and the subsequent methane premixed flame ignition, a constant volume configuration relevant to pilot-ignited dual fuel engines, was investigated by DNS. It was found that reducing the pilot fuel quantity, increases its autoignition time. This is attributed to the faster disappearance of the most reactive mixture fraction (predicted from homogeneous reactor calculations) which is quite rich. Consequently, ignition of the n-heptane occurs at leaner mixtures. The premixed methane flame is eventually ignited due to heating gained by the pressure rise caused by the n-heptane oxidation, and heat and mass transfer of intermediates from the n-heptane autoignition kernels. For large amounts of the pilot fuel, the combustion of the n-heptane results in significant adiabatic compression of the methane-air mixture. Hence the slow methane oxidation is accelerated and is further promoted by the presence of species in the oxidizer stream originating from the already ignited regions. For small amounts of the pilot fuel intermediates reach the oxidizer stream faster due to the very lean mixtures surrounding the n-heptane ignition kernels. Therefore the premixed methane oxidation is initiated at intermediate temperatures. Depending on the amount of n-heptane, different statistical behaviour of the methane oxidation is observed when this is investigated in a reaction progress variable space. In particular for large amounts of n-heptane the methane oxidation follows roughly an autoignition regime, whereas for small amounts of n-heptane methane oxidation is similar to a canonical premixed flame. The data can be used for validation of various turbulent combustion models for dual-fuel combustion.

Keywords: Dual fuel combustion, autoignition, n-heptane spray, premixed methane, propagation

1. Introduction

Reciprocating engines is an important and growing area for natural gas utilization due to the lower NO_x, CO_2 and soot emissions achieved [1–3] . The small propensity of natural gas to autoignite allows high intake pressures and high compression ratios with turbochargers [1, 3, 4], which then allows high thermodynamic efficiencies [1, 3, 5]. Small natural gas engines are typically ignited by a spark [3, 6]. However, large-bore engines as in power generation and the marine engine sector, where the pressure at the time of ignition is high, are typically ignited by a pre-chamber and a jet [7, 8], or by a pilot injection of a liquid fuel which is easy to autoignite [1, 3–5]. Essentially, the ignition centres of the pilot fuel provide the energy required for the initiation of the gasous premixed flame [5, 6, 9–11]. This second mode of ignition, which involves autoignition of a pilot spray in a oxidizer that is already mixed with another fuel is studied in this paper from a fundamental perspective.

There is only limited work in the context of simulations and experiments for this complex problem. From a practical perspective, previous research has focused on rapid compression machines [11, 12] and single cylinder four stroke direct injection engines [2, 10, 13, 14]. One of the key findings was that ignition of the pilot spray is retarded in the presence of methane [2, 11, 12, 14], and that OH* chemiluminescence intensity is increased, indicating an active role of methane in the combustion process [10, 11]. It was also observed that increasing the number of holes in the liquid fuel injector enhances methane consumption [11, 15] due to the larger number of the pilot fuel ignition centres that were available. In an effort to enhance the knowledge from the experimental observations various numerical approaches have been attempted aiming to model the combustion of a gaseous fuel mixed with air, ignited by the injection of a higher hydrocarbon fuel under engine relevant conditions [15–17], but there is very limited use of advanced turbulent combustion models. Schlatter et al. (2011) [16] used a two-dimensional Conditional Moment Closure (CMC) formulation and defined the hot spots predicted from the CMC model as the initial kernels of a premixed flame model [16]. However, since the ignition spots were simplified as premixed flame kernels, the exact mechanism causing the premixed methane flame initiation and the extent to which the flame is sustained was not examined. The structure of premixed flames in a conditioning-variable space, as in CMC, has been explored [18, 19], but ignition of such flame through second fuel autoignition has not been studied.

The description of the combustion of a gaseous fuel in the presence of a higher hydrocarbon fuel poses another challenge, the choice of the chemical scheme to implement in order to model the

simultaneous oxidation of both fuels. Various attempts have been reported in order to construct computationally viable mechanisms under engine relevant conditions; for example Khalil et al. (1996) examined a detailed scheme and derived a reduced scheme [9]. Conversely, Maghbouli et al. (2013) added oxidation paths of methane to an existing mechanism of higher hydrocarbon (n-heptane) in order to facilitate dual fuel investigations [17]. Schlatter et al. (2011) [16] used a chemical mechanism validated for n-heptane autoignition (pilot fuel) which contains methane [20], but it was not verified whether this can adequately describe the methane oxidation.

Apart from simulations based on RANS and the above-mentioned preliminary experiments there is no fundamental study of dual fuel combustion with two-phase turbulent combustion simulations. Direct Numerical Simulations (DNS) have proven to be a valuable tool for providing information on the autoignition and spark ignition of turbulent sprays [21–26]. Nevertheless the second fuel in the oxidiser is expected to alter the way autoignition kernels develop as reviewed in Ref. [27] and in greater extent the propagation in a gas-fuelled premixed mixture. The dual fuel combustion problem can also be thought of as an extension of the turbulent premixed flame problem in the sense that the hot kernel comes from liquid fuel autoignition rather than heat addition to a fluid of homogeneous composition [28, 29]. Notwithstanding the information provided by DNS of turbulent spray combustion and premixed flame investigations, the dual fuel combustion case is characterised by complex flame structures featuring both non-premixed autoignition and premixed flames [30] and the fundamentals of these processes have not been studied in the necessary detail before [3].

The specific objectives of this work are: (i) to investigate the fundamentals of liquid fuel (n-heptane) autoignition in the presence of methane; (ii) to demonstrate how the autoignition of the n-heptane is affected by the amount of the liquid fuel; and (iii) to investigate the premixed methane flame initiation mechanism and how this is affected by the amount of n-heptane. This investigation is performed in the context of two phase DNS using complex chemistry. The pilot fuel quantity is varied while the temperature, turbulence intensity, and premixed methane equivalence ratio are kept constant.

2. Mathematical formulation

2.1. Overview

The details of the code and the governing equations have been described in previous works considering spark ignition of turbulent sprays [22, 23] and autoignition of turbulent sprays under high pressures and intermediate temperatures [24, 31]. Therefore the governing equations for the liquid and gaseous phases are provided here as Supplementary Material for the interested reader for the purposes of completeness. In summary, the liquid phase consisted of n-heptane droplets and was treated with the Lagrangian point-source approximation assuming uniform temperature within the droplet. The droplet evaporation rate and the amount of heat exchanged with the gaseous phase were computed based on the thin film assumption [32]. The physical properties of the air/vapor mixture in the film were evaluated according to the 1/3 rule [33]. For each droplet a set of equations was solved in order to determine its position, velocity, diameter, and temperature [34]. The droplet Spalding numbers for heat and mass transfer appearing in the liquid phase governing equations were evaluated according to [34] and are variable with time. Regarding the gaseous phase, fully compressible fluid is considered. The temporal and spatial evolution of the gaseous phase is described by the continuity of mass, momentum, internal energy, and $N_s - 1$ transport equations for conservation of species mass fraction, where N_s is the number of species for which transport equations are solved. The Lewis number is assumed to be equal to unity for all the species. The heat capacity and enthalpy for the species are evaluated using fifth order polynomials provided by [20]. In order to account for the changes in mass, momentum, and energy due to evaporation a liquid source term appears in the gaseous-phase governing equations. The liquid source terms are assigned to the gaseous phase up to a cut-off, according to a distance function which decreases exponentially with increasing distance from the centre of the droplet [21–24]. Complex chemistry is employed and the various reaction rates are computed according to the Liu et al. (2004) mechanism [20]. Validation for the implementation of the particular chemical scheme is discussed in section 2.3 and in the Appendix.

2.2. Numerical procedure

The governing equations were solved using the three-dimensional compressible DNS code SENGA2, previously used for a variety of turbulent combustion problems [22–24, 35, 36]. A tenth-order explicit central difference scheme was employed for the computation of the first and second order

spatial derivatives [37]. In order to enable the calculation of stiff chemistry, operator splitting between transport and chemistry was implemented. Application of operator splitting in DNS was studied and validated in previous investigations [38, 39]. The transport is solved explicitly while the chemical source contribution is solved by a stiff ODE integrator. In particular, the gaseous-phase and liquid-phase transport equations were advanced using a fourth-order, low-storage explicit Runge-Kutta scheme [40] with a time step $\Delta t = 5.0 \times 10^{-9}$ s, while the implicit solver VODPK [41] was used for advancing in time the gas-phase chemical reactions. The time step was chosen to be smaller than the acoustic time scale in a grid cell ($\Delta x/\sqrt{\gamma(R/W_{air})T}$), which represents the smallest non-chemical time scale in the simulation.

2.3. Chemical Mechanism

The reduced mechanism of Liu et al. (2004) [20] was used containing 22 non steady-state species and 18 global steps. The reduced mechanism was derived from a skeletal mechanism consisting of 43 species and 185 reactions. It was validated by Liu et al. (2004) [20] in terms of the ignition delay time of homogeneous heptane mixtures using the experimental data of Ciezky and Adomeit (1993) [42]. The scheme has been used previously for heptane autoignition problems [23, 24, 43, 44] and contains methane. A parametric study was performed to examine the behaviour of the mechanism under different equivalence ratios of methane in air, pressures and temperatures considering adiabatic homogeneous n-heptane/oxidizer mixtures, with the oxidizer being a methane/air mixture (see section 3). Homogeneous reactor calculations were also performed using the skeletal scheme [20] and are presented in Appendix A.1. In general, the ignition delay time and most reactive mixture fraction values predicted by the reduced scheme follow the same trend and only differ about 5 % from the values given by the skeletal scheme. In order to examine if the mechanism employed is also representative of methane combustion, one-dimensional laminar premixed flame calculations were performed with the skeletal scheme using the Cosilab package [45] (see Appendix A.2). The laminar flame speeds and species profiles were compared with the corresponding profiles predicted by the GRI-3.0 mechanism [46] at the DNS conditions. Results are qualitatively and quantitatively similar for the two chemical mechanisms as discussed in Appendix A.2. The reduced scheme [20] was also used to model the ignition and combustion of a heptane spray in a lean premixed methane/air mixture [11]. The agreement was reasonably good and the trend observed in the experiment was reproduced in the numerical investigation. Therefore the Liu et al. (2004) scheme is able to describe reasonably well the methane premixed flame once initiated for the purposes of this work.

2.4. Simulation parameters and problem set-up

In the present study, the cubic domain had a length of $L = 2.4$ mm and uniform grid spacing resolution of 23 μm resulting in 104 grid nodes in each direction. A grid independence analysis performed *a posteriori* on the DNS data set is presented in Appendix B. The initial ambient pressure was $P_0 = 24$ bar and the temperature of the oxidizer stream was 1050 K. The pressure chosen is lower than what is usually encountered in diesel engines, but it is also below the critical pressure of n-heptane ($P_c = 27.6$ bar [47]). Under supercritical conditions, the evaporation model may not be valid [47], hence subcritical pressure is initially considered in this work. Additionally, similar temperature and pressure values were also used in previous numerical investigations of spray autoignition in HCCI engines [24] and experimental investigations of dual fuel engines [2] suggesting that the conditions investigated are plausible. Periodic boundary conditions were applied to all spatial directions therefore mimicking constant volume configuration. The oxidizer stream consisted of air and methane at an equivalence ratio of 0.6.

The turbulent velocity field was initialised according to a Batchelor-Townsend [48] energy spectrum with integral length scale l_t of the order of $L/6$. The turbulence was isotropic and decaying, and there was no initial mean flow. The initial turbulent velocity fluctuation magnitude was $u'_0 = 0.78$ m/s and the turbulent Reynolds number $Re_t = u' l_t/\nu = 60$. The Re_t employed in this study is similar to the Re_t employed in several previous studies of turbulent spray autoignition and turbulent premixed flames [22–25, 28, 29]; although it might be low compared to the Re_t encountered in practical applications, it is considered as a feasible realisation of a combustion mode that has not been studied before by high fidelity simulations. Examination of the temporal evolution of the turbulent kinetic energy, the energy dissipation, and the integral length scale (not shown here) revealed that the turbulence decays as expected and that when the premixed flame is initiated the turbulent Reynolds number has fallen to about one third of its initial nominal value. The initial value of the Kolmogorov length scale was $\eta_K = 25.2\,\mu$m, indicating that the turbulence was well resolved. The initial droplet velocity was set equal to that of the background carrier-phase and the droplet temperature was $T_F = 450$ K. The initial droplet diameter was set equal to 25 μm in all simulations.

Two cases were simulated that differed in the amount of n-heptane and hence number of droplets. The amount of n-heptane was described by the parameter R:

$$R = \frac{m_{C7} LCV_{C7}}{m_{C7} LCV_{C7} + m_{C1} LCV_{C1}} \tag{1}$$

where m_{C7} represents the total mass of n-heptane in the domain and m_{C1} the total mass of methane. The Lower Calorific Values of n-heptane (LCV_{C7}) and methane (LCV_{C1}) are 44.926 MJ/kg and 50.016 MJ/kg respectively [49]. For case A, $R_A = 0.55$ whereas for case B, $R_B = 0.16$. The two cases also differed in the spatial distribution of the droplets: for case A they were randomly distributed in a layer extending from $x = 0.35L$ to $x = 0.65L$, whereas for case B they were randomly distributed in a sphere with its centre at the centre of the domain and radius equal to $0.185L$ (as illustrated in Fig. 1). Thus the two cases also differ in the overall equivalence ratio in the droplet laden region, Φ_0 (Eq. (2)), which is equal to 2.08 for case A and 4.4 for case B.

$$\Phi_0 = \frac{\frac{nm_d}{(m_{ox})_d}}{(\frac{m_{C_7H_{16}}}{m_{ox}})_{st}} \tag{2}$$

where n is the number of droplets and m_d is the initial mass of each droplet (mono-disperse spray is considered here). The mass of the oxidizer $(m_{ox})_d$ considered for the computation of Φ_0 refers to the oxygen present in the droplet laden region. The denominator represents the ratio of the mass of n-heptane over the mass of oxygen at stoichiometry, $(\frac{m_{C_7H_{16}}}{m_{ox}})_{st} = 0.284$. Details for the simulations investigated are outlined in Table 1 together with the evaporation time (τ_{evap}) and eddy turn-over time (τ_{turb}). The τ_{evap} is taken as the time when all droplets evaporated, evaluated as in [34].

The cases investigated offer a solid ground to deduce conclusions on the behaviour of the system for different amounts of n-heptane. It is of interest to study cases that differ in the amount of the pilot fuel quantity, i.e. with different R because the different R may lead to different adiabatic compression of the methane/air mixture. Consequently, the methane/air mixture may autoignite rather than burn by flame propagation. This phenomenon is broadly identified as knock of the dual fuel engine [3, 10], caused by excessive pressure rise associated with the pilot fuel quantity. Furthermore, the configurations chosen will not affect the primary goal of this study which is to investigate the physics of liquid fuel autoignition and the ensuing flame propagation. Finally the resulting equivalence ratio ensures the existence of adequate amount of n-heptane in the droplet laden region in order to produce favourable conditions for ignition for both cases.

In processing the numerical results, a mixture fraction ξ based on the nitrogen mass fraction, Y_{N_2}, was used ranging between 0 in the oxidizer stream (i.e. $\xi = 0$ refers to the methane/air mixture) and 1 in the n-heptane, namely

$$\xi = \frac{Y_{N_2} - Y^o_{N_2}}{Y^F_{N_2} - Y^o_{N_2}} \tag{3}$$

where $Y^o_{N_2}$ is the value of Y_{N_2} in the oxidizer stream and $Y^F_{N_2}$ the value of Y_{N_2} in the fuel stream (n-heptane). In order to investigate the premixed flame evolution, a progress variable based on the methane mass fraction was introduced, which conditioned at $\xi = 0$ gives:

$$C(\xi = 0) = \frac{Y^{inert}_{CH_4} - Y_{CH_4}}{Y^{inert}_{CH_4}} \tag{4}$$

Hence, $C = 0$ means that the methane present in the methane/air stream has not reacted yet, whereas $C = 1$ indicates fully burnt methane.

3. Results

3.1. Autoignition of homogeneous mixtures

Calculations of the ignition delay time in homogeneous systems provide useful insights for understanding the physics of autoignition in turbulent sprays [27]. In this context, calculations of the ignition delay time of homogeneous n-heptane/oxidizer mixtures were performed, with the oxidizer being a mixture of air and methane at a given equivalence ratio (ϕ_{CH_4}). The initial temperature and composition in mixture fraction space ($0< \xi <1$) is computed assuming inert mixing between the n-heptane and the oxidizer stream following the methodology proposed in [50] and discussed in [27]. The temperature of the oxidizer stream (ξ=0) is 1050 K whereas the temperature of the n-heptane (ξ=1) is 450 K and pressure is either 24 bar or 40 bar. Autoignition was defined as the time when the temperature reached 1250 K.The same criterion was used for the DNS results discussed later. This method of setting a temperature cut-off to define autoignition was previously used in DNS of spray autoignition [24, 31] and in other numerical investigations of dual fuel combustion [16]. Setting a different temperature value to define autoignition would not cause any appreciable change in the ignition delay time due to the rapid increase of temperature at ignition. For each set of conditions, the shortest ignition delay time, τ_{id}, is observed for a composition defined as the most reactive mixture fraction (ξ_{MR}).

The resulting ignition delay times are presented in Fig. 2. Comparison of the ϕ_{CH_4}=0 and ϕ_{CH_4}=0.6 cases indicates that increasing the amount of methane in the oxidizer stream, increases the value of the τ_{id} and shifts the value of the ξ_{MR} to richer mixtures, see also Table 1. Considering the ϕ_{CH_4}=0.6 curves at 24 bar and 40 bar, the ignition delay time increases significantly for both cases while approaching $\xi = 0$, i.e. the ignition time of the premixed methane/air mixture ($\tau_{id,0}$) is significantly longer than the ignition time of the n-heptane/oxidizer mixture. This is the main

feature of pilot ignited natural gas engines [3, 12] which is therefore reproduced by the chemical mechanism employed. The ignition delay time is also sensitive to pressure as depicted in Fig. 2.

In order to investigate the effect of pressure and methane content on $\tau_{id,0}$, homogeneous reactor calculations were performed for a wide range of ϕ_{CH_4} under different pressures and the results are illustrated in Fig. 3. The ignition delay at $\xi = 0$ ($\tau_{id,0}$) is over one order of magnitude higher than the value of τ_{id} observed in Fig. 2. This behaviour was also observed in previous experimental [12] and numerical investigations using detailed chemical schemes [9]. Increasing pressure reduces the ignition delay time of methane (Fig. 3). In constant volume systems, due to the combustion of n-heptane at richer mixtures ($\xi > 0$), the methane/air mixture is subject to increased temperatures in addition to increased pressures due to adiabatic compression. It is therefore necessary to investigate the $\tau_{id,0}$ under increased temperature and pressure conditions. Setting the final pressure $P_{fin} = 38$ bar (equal to half of the maximum pressure observed in the DNS - case A) and performing adiabatic compression from 24 bar to 38 bar (T_{fin}=1200 K), a reduced ignition delay time is determined and plotted in Fig. 3. The resulting $\tau_{id,0}$ under the above-mentioned conditions is significantly shorter than $\tau_{id,0}$ under the nominal initial conditions (T=1050 K, P=24 bar). Consequently, if the pressure and temperature rise are high enough, methane might autoignite rather than burn by premixed flame propagation. Note that the value of R (Eq. (1)) will crucially affect the level of adiabatic compression.

In order to examine the effect of the presence of methane in the oxidizer stream on the autoignition of n-heptane, τ_{id} and ξ_{MR} are plotted for a range of equivalence ratios of methane (ϕ_{CH_4}) in Fig. 4. It is evident that ignition of n-heptane in the presence of methane is retarded and that increasing the ϕ_{CH_4} increases the τ_{id} further. This is consistent with previous experimental [11, 12, 14] and numerical [9, 16, 17] investigations that revealed the inhibiting effect of methane on the ignition delay time of n-heptane. However, increasing pressure makes the ignition delay time of n-heptane less sensitive to changes in ϕ_{CH_4}. This is more pronounced at high temperatures for the range of the equivalence ratios investigated. For example at P=40 bar, the ignition delay time of n-heptane is increased by 42% for T=850 K (increasing ϕ_{CH_4} from 0 to 2.0), whereas for T=1050 K this increase is no more than 16%. In addition, increasing ϕ_{CH_4}, shifts the autoignition of n-heptane to richer mixtures as depicted by Fig. 4. Increasing the oxidizer temperature (from 850 K to 1050 K) results in even richer most reactive mixture fractions because they correspond to higher initial temperature. In particular ignition at 850 K occurs close to the stoichiometric mixture fraction (ξ_{st} evaluated as [51]) whereas for 1050 K, ignition occurs around $3\xi_{st}$. Nevertheless, there seems to

exist an upper limit on how rich ξ_{MR} could be for low pressures as captured from the curve at 10 bar. This trend is also present for even lower pressures (not shown here).

3.2. DNS Results

3.2.1. General remarks

The temporal evolution of the volume averaged temperature and pressure is shown in Fig. 5. Due to the higher amount of n-heptane, the volume averaged temperature of case A is significantly affected by cooling due to evaporation. However, this temperature drop is soon overcome, and case A undergoes thermal runaway earlier than case B as also shown by the corresponding pressure traces. Furthermore, the temperature and pressure rise during the thermal runaway, is steeper for case A than for case B. From such volume-averaged quantities, ignition may be considered to occur at about 1.2 ms, which is longer than the minimum ignition time of n-heptane/methane-air mixtures observed in Fig. 4. The time of appearance of the first ignition spot in the turbulent flow is compared to τ_{id} later (Section 3.2.3). The remainder of this work is dedicated to a detailed description of n-heptane autoignition and premixed methane flame initiation.

3.2.2. Pre-ignition phase

Prior to ignition, droplet evaporation and mixing of the fuel vapour with the ambient air are the dominant processes. Once a reactive mixture is formed, the heat release rate starts to be significant [24]. Figures 6 and 7 show the distribution of heat release rate (HRR), CH_4 reaction rate, scalar dissipation rate (N) and mass fractions of CH_2O, OH, and HO_2 in mixture fraction space early before ignition, at $t = 0.650$ ms. It is evident that case A exhibits higher scalar dissipation rates, especially in the range $0.1 \leq \xi \leq 0.2$. The greater number of droplets with the combination of lower Φ_0 introduces a larger number of evaporation centres and significant stratification of the mixture and hence mixture fraction gradients. The high scalar dissipation at $0.1 \leq \xi \leq 0.2$ coincides with the corresponding lower values of the heat release rate and the production rates of the intermediate species. Methane is produced for $0.07 \leq \xi \leq 0.15$, where mass fractions of CH_2O, OH, and HO_2 peak, while it is being consumed for $\xi < 0.07$ and $\xi > 0.15$. This behaviour of alternate consumption and production is a result of the impact of temperature, oxygen and the competition between the two fuels: the n-heptane and the methane. At lean mixture fractions ($\xi < 0.07$) the high temperature and high concentration of methane results in the consumption of methane. At the other extreme, i.e. $\xi > 0.15$, the temperature range falls within the low temperature regime for oxidation of

methane favoured in the presence of oxygen [52]. Intermediate mixture fractions contribute to the formation of a pool of radicals (OH, HO_2) and intermediate species (CH_2O) [24] and methane appears also as part of the oxidation path of n-heptane. It worth noting the finite concentration of OH near the $\xi \approx 0$ regions depicting the early but very slow oxidation of methane present in the oxidizer stream. The complexity of the pre-ignition period stems from the simultaneous occurrence of physical (evaporation) and chemical processes and their mutual interactions generating mixture fraction gradients as suggested by the scalar dissipation rate distribution.

Since there is a lot of scatter and the chemical rates span several orders of magnitude it is better to parametrize the early stages conditioned both on mixture fraction and scalar dissipation rate [53]. The doubly conditioned heat release rate is plotted in Fig. 8 for different time instants for the indicated values of scalar dissipation. Higher heat release rate is associated with low values of scalar dissipation for both cases, as observed in previous investigations of n-heptane autoignition [24]. Initially, case B exhibits higher heat release rates as it is less affected by evaporative cooling. However, as time advances, this trend is compensated by the smaller amount of n-heptane and, by the time the system undergoes the runaway, rich mixtures do not exist. Figure 8 also demonstrates that while high heat release rate in rich mixtures occurs for low values of scalar dissipation, at lean mixtures the main contribution of heat release rate comes from higher scalar dissipation regions of the flow.

3.2.3. Ignition phase

As revealed from Fig. 8, the system is evolving towards ignition with the heat release rate increasing significantly around $\xi = 0.21$. This is close to the value predicted from the homogeneous reactor calculations (Fig. 2), as previously observed in autoignition of turbulent sprays in air [24, 25]. Indeed, ignition for case A occurs at $\tau_{id}^{DNS,A} = 1.035$ ms, at $\xi = 0.213$ as depicted in Fig. 9 showing scatter plots of temperature, CH_4 reaction rate, and mass fractions of O_2 and OH. Rapid depletion of O_2 and formation of radicals is quite concentrated in mixture fractions around ξ_{MR}. Methane is consumed at the ignition location and the consumption rate is several orders of magnitude higher than any activity near the $\xi \approx 0$ region, which in turn appears to be negligible. The scatter plots of case B at the ignition time (Fig. 10) reveal a different behaviour: high temperature regions span over greater range of mixture fraction values, albeit lower than ξ_{MR}. Ignition for case B occurs at $\tau_{id}^{DNS,B} = 1.148$ ms around $\xi = 0.15$ as shown in Fig. 10. The picture emerging in physical space is that autoignition is characterized by localized kernels originating from rich mixtures, that grow

and expand into leaner mixtures. Figure 11 shows the temperature iso-surface of $T = 1250$ K soon after ignition coloured according to the mixture fraction. Localized autoignition kernels are evident for both cases. Due to the composition of case B which involves leaner mixtures, only one kernel is evident that is surrounded by very lean mixtures. Indeed, the T=1250 K iso-surface of case B expands to leaner mixtures than for case A, approaching mixtures with $\xi \approx 0$, even though ignition for case A occurred earlier ($\tau_{id}^{DNS,A} < \tau_{id}^{DNS,B}$). Figure 12 shows the probability of finding mixtures with composition equal to ξ_{MR} and the corresponding conditionally averaged temperature. Since ξ_{MR} is quite rich, a significant amount of liquid fuel needs to be evaporated and ξ_{MR} first appears after 0.2 ms for both cases. The temperature then increases, but ξ_{MR} for case B is lost prior to the steep rise, due to mixing caused by turbulence [31]. Therefore, ignition shifts to leaner mixtures resulting in a longer ignition delay time compared to case A. Both cases ignite later than τ_{id} (Table 1) due to a combination of finite scalar dissipation and evaporative cooling as previously observed for autoignition of turbulent sprays in air [24].

3.2.4. Propagation in mixture fraction space

The temporal evolution of conditionally averaged temperature, CH_4, CH_2O and OH mass fractions, denoted as $\langle T|\xi\rangle$, $\langle CH_4|\xi\rangle$, $\langle CH_2O|\xi\rangle$ and $\langle OH|\xi\rangle$ respectively, are shown in Fig. 13, conditioned on mixture fraction. As time progresses and mixing occurs, the mixture fraction range and scalar dissipation values are reduced. After ignition, the peak temperature increases and moves to leaner mixture fractions for both cases. Consistent with the profile of $\langle T|\xi\rangle$, the peak of $\langle OH|\xi\rangle$ increases and moves to leaner mixtures. The higher peak temperature for case A at the last instant plotted, t_5=1.47 ms, is associated with higher peak in the $\langle OH|\xi\rangle$ distribution. Greater CH_4 consumption is observed for case B. This is attributed to the early higher activity of case B (as observed in Figs. 7 and 8) promoting early consumption of methane and to the autoignition of n-heptane occurring at leaner mixtures (Fig. 10) compared to case A (Fig. 9). When autoignition of n-heptane occurs in rich mixtures oxygen and other radicals are not sufficient for the combustion of both n-heptane and methane. Therefore some methane survives (captured in Fig. 13), which could contribute to the so-called "methane slip" observed in actual gas engines [10]. The temporal evolution of $\langle CH_2O|\xi\rangle$ is similar for both cases; $\langle CH_2O|\xi\rangle$ first peaks at the ignition location and this peak moves progressively to leaner mixtures while the peak value is decreasing. However, at the last instant plotted the CH_2O mass fraction spans over greater range of mixture fraction for case B, whereas for case A, CH_2O is found only for ξ <0.02. At the last instant plotted (t_5=1.47

ms), $\langle T|\xi = 0\rangle$ for case A has increased compared to the corresponding temperature for case B, indicating premixed methane ignition. This might be attributed to the adiabatic compression as the pressure has risen due to the n-heptane combustion (Fig. 5), but also due to diffusion of heat and radicals from the already ignited regions initiating the premixed flame. The contributions of these two phenomena are explored in the next section.

3.2.5. Premixed flame initiation

In order to examine whether methane in the oxidizer stream has ignited, a $\tau_{id,0}^{DNS}$ is defined as the time when T=1250 K is reached in the $\xi = 0$ fluid, with $\xi = 0$ being defined in the window $0 \leq \xi \leq$0.005. Consequently, $\tau_{id,0}^{DNS,A} = 1.315$ ms whereas $\tau_{id,0}^{DNS,B} = 1.290$ ms. Therefore the higher $\langle T|\xi = 0\rangle$ of case A observed in Fig. 13 is not indicative that ignition at $\xi = 0$ occurred earlier as this is an average quantity and the cases investigated are subject to different adiabatic compression.

The contribution of the mechanisms involved in the premixed flame initiation is illustrated in Fig. 14 which shows the temporal evolutions of $\langle T|\xi = 0\rangle$, $\langle \mathrm{OH}|\xi = 0\rangle$ and $\langle \mathrm{RR.CH_4}|\xi = 0\rangle$ (where RR stands for reaction rate). During the early stages of evaporation and mixture formation, the decrease of temperature due to evaporative cooling is more significant for case A resulting in higher heat release rates for case B (as seen in Fig. 8). As time advances, the temperature rise for case A occurs earlier and is steeper (as showed in Fig. 5) because n-heptane autoignition occurs earlier (Fig. 9), leading to higher pressures and temperatures than case B for $t > 1.2$ ms. This is reflected to the temporal evolution of the average temperature in the oxidizer stream ($\langle T|\xi = 0\rangle$) shown in Fig. 14. Hence, $\langle T|\xi = 0\rangle$ of case A reaches the ignition threshold (1250 K) earlier which is consistent with the observation of Fig. 13. Figure 14 shows OH mass fraction and CH_4 reaction rate at $\xi = 0$ in a representative window after n-heptane autoignition (1.3 ms$\leq$ t $\leq$ 1.4 ms). The ignition kernels of case B are surrounded by very lean mixtures (see Fig. 11) and therefore OH reaches the $\xi = 0$ region earlier than for case A, which explains the slightly earlier consumption of methane observed. On the contrary, minor methane consumption is observed for case A before significant accumulation of OH ($t \leq 1.35$ ms). This is favoured due to the higher temperatures observed because of the higher amount of n-heptane that has burnt, which in turn promotes oxidation of methane. Once OH reaches the $\xi = 0$ region, methane consumption for case A is accelerated. Hence, methane oxidation largely depends on both mass transfer from richer mixtures ($\xi > 0$) and pressure rise and increased temperatures due to n-heptane autoignition. If R is very small, the pressure effect will be negligible, but if R is large it can be dominant and then the methane/air mixture may knock [3].

Contours of mixture fraction with super-imposed iso-lines of OH mass fraction for case B, taken at $x = 0.79L$ at $t = 1.32, 1.40, 1.48$ ms, are illustrated in Fig. 15. The ignition kernels are surrounded by OH which is intensified at the interfaces between the ignition kernels and methane/air mixture ($\xi = 0$). The temporal evolution of OH contours reveals that apart from propagation to rich mixtures, OH migrates from ignition kernels to the premixed methane/air mixture. Methane oxidation at $\xi = 0$ is then initiated in the neighbourhood of the ignition kernels as captured in Fig. 16, which shows the growing outline of the thin premixed flame front visualized by the iso-surface of $C = 0.5$ (see Eq. (4)).

3.2.6. Discussion on the two modes of methane consumption

It was previously shown that during n-heptane autoignition, methane is slowly consumed (Figs. 6 and 7). In addition, n-heptane ignition kernels at finite ξ, supply the $\xi = 0$ region with intermediates necessary for methane oxidation (Figs. 14 and 15). These two mechanisms constitute the components for the description of the phenomena occurring at $\xi = 0$. In this context, various scalars from the DNS are plotted in Figs. 17 and 18 (for case A and B respectively) as a function of the progress variable C and compared with homogeneous reactor calculations and 1-D laminar premixed flame calculations evaluated at the composition of $\xi = 0$ (ϕ_{CH_4}=0.6). The definition of progress variable C for homogeneous reactor and premixed flame calculations is based on the inert value of methane mass fraction found at $\phi_{CH_4} = 0.6$, which is identical to Eq. (4).

The DNS data taken from case A correspond to $t = 1.47$ ms and the data from case B correspond to $t = 1.4$ ms. The time instant chosen must satisfy two criteria: it first has to be well after the premixed flame initiation so that an adequate amount of points exist in the $0 \leq C \leq 1$ region, and secondly to be well before total methane consumption so that enough points of intermediate methane consumption exist. The pressure at t=1.47 ms for case A has reached 70 bar whereas the pressure for case B at t=1.4 ms has reached 27 bar. The corresponding temperature resulting from adiabatic compression (T_{ad}) for case A (from P_0=24 bar to P_{fin}=70 bar) is 1425 K, and for case B (from $P_0 = 24$ bar to $P_{fin} = 27$ bar) it is 1080 K. The resulting set of conditions (P_{fin}, T_{ad}) were used for the homogeneous reactor and premixed flame calculations. Under these conditions, the ignition delay time predicted from homogeneous reactor calculations is 0.12 ms for case A and 10.53 ms for case B. It should be noted that under markedly high pressures (e.g. $P = 70$ bar) and temperatures (e.g. $T = 1425$ K) the concept of laminar premixed flame may be questioned, as it is associated with short residence time and thin preheat zone. However, using an adequately thin preheat zone,

such calculations are provided for comparison to the homogeneous reactor and DNS set of data points. Unity Lewis number is assumed in order to be consistent with the DNS data. The laminar premixed flame species profiles associated with the above conditions are expected to be quite thin and hence the grid resolution initially implemented may be questioned. Notwithstanding the initial resolution limitation, the conclusions drawn from the grid independence discussion presented in Appendix B demonstrate that the coarse and fine grid scatter plots of various quantities versus progress variable have very similar behaviours.

In general, the scatter plots of case A (Fig. 17) follow the behaviour of a homogeneous reactor undergoing autoignition rather than the premixed flame concept, whereas the scatter plots of case B (Fig. 18) reveal a more complex behaviour falling between these two canonical flame concepts. To start with, heat release rate of case A follows the homogeneous reactor profile whereas premixed methane flame calculations predict higher values of heat release rate that peaks at a slightly lower value of C. With regard to case B, the heat release rate profiles for the homogeneous reactor, premixed flame, and DNS results are quite similar both qualitatively and quantitatively, suggesting that the higher heat release reactions originate in the range of $0.7 \leq C \leq 1.0$. Furthermore, the premixed flame and homogeneous reactor calculations reproduce quite well the temperature profile of the DNS data for case B. However, for $0.4 \leq C \leq 0.8$ the temperature of the DNS seems to be higher than what would be encountered if the methane was undergoing autoignition. It is also higher than the temperature from the premixed flame, indicating the contribution of heat transfer from the already ignited n-heptane regions. The temperature observed in the DNS data set of case A (Fig. 17) is lower compared to the homogeneous reactor and premixed flame profiles especially for low values of C. This is because adiabatic compression gives higher temperature than what is encountered in the DNS. Nevertheless, increasing C, the temperature of the DNS seems to follow the homogeneous reactor profile.

Regarding the methane consumption rate, the scatter plot of case A closely follows the homogeneous reactor profile. With regards to case B, the premixed flame calculations predict the consumption peak at a slightly lower value of the progress variable C. The consumption peak predicted by the homogeneous reactor calculations coincides with the peak observed in the DNS, although the maximum consumption value is under-predicted. This is consistent with the lower temperature observed, especially in the range $0.4 \leq C \leq 0.8$. Hence, the profile of the DNS data set of case B, is closer to the premixed methane flame profile against the progress variable C.

According to the mechanism and temperature range considered here, the chain initiation step

for methane oxidation is thermal decomposition, which produces H and H_2, initiating the $H_2 - O_2$ chain. Then a pool of O, OH, and H develops which abstracts H from CH_4 producing CH_3 [20, 52]. The profiles of CH_3 reaction rate and mass fraction for case A, coincide with the homogeneous reactor profile. Considering case B, the reaction rate of CH_3 between $0.6 \leq C \leq 0.9$ (DNS data) is lower than the premixed flame predictions and yet the DNS profile of CH_3 is qualitatively similar to what is expected for a premixed methane flame. This indicates that the presence of CH_3 in the $\xi = 0$ (case B) may be attributed to the mass transfer from the n-heptane kernels.

Significant production of HO_2 is evident in the window $0.3 \leq C \leq 0.6$ especially for case B, which is not predicted from homogeneous reactor or premixed methane flame calculations. This is reflected in the profile of HO_2 mass fraction in the above-mentioned window of C. Higher mass fraction of HO_2 in the DNS for both cases is also encountered near C=0 compared to the homogeneous reactor and premixed flame calculations. For slightly higher value of C the scatter plot of case A seems to follow the homogeneous reactor profile while for case B a more complex behaviour is observed.

The presence of CH_3 leads to the formation of CH_2O [20, 52], which will finally give CO and CO_2 [13]. The scatter plots of CH_2O mass fraction fall between the premixed flame profiles and the homogeneous reactor profiles for both cases, although the DNS data set of case A is much more closer to the homogeneous reactor profile. This behaviour was expected as the CH_2O reaction rate of case A is also quite similar to the homogeneous reactor profile. The reaction rate of CH_2O for case B reveals a different behaviour which is reflected to the distribution of CH_2O mass fraction against C. In particular, the CH_2O mass fraction remains higher than the premixed flame profile even for $0.4 \leq C \leq 0.85$ when production rate is lower suggesting mass transfer from $\xi > 0$. Higher CH_2O mass fraction is observed for homogeneous reactor calculations as the induction time for that system lasts for more than 10 ms during which CH_2O is accumulated. Therefore, the high mass fractions of CH_2O observed near C=0 (although less prominent for case A) may be explained as a consequence of the slow methane autoignition, which was virtually initiated at $t = 0$ ms.

The methane and oxygen gradients in the oxidizer stream are important for the identification of methane consumption centres in physical space. Due to the nature of the premixed methane oxidation regime of case A, these gradients are lower compared to case B but in general they follow the same trend. Hence the corresponding gradients of case B are considered in the following. The scatter plots of the dissipation of the key species (CH_4 and O_2) for case B against the progress variable C are plotted in Fig. 19 (conditioned on $\xi = 0$). In principle, the gradients follow the premixed flame profile but they differ for $0.9 \leq C \leq 1.0$, where the decrease to zero is sharper for

the DNS. This difference is also observed in the CH_4 gradients. Also, the premixed profile suggests higher gradients between $0.6 \leq C \leq 0.9$, but for DNS this transition is smoother. It is worth noting, that both species reveal the presence of unreacted ($C = 0$) methane/air ($\xi = 0$) regions, with high gradients. This suggests the presence of $\xi = 0$ fluid around the n-heptane ignition kernels, which was previously discussed and identified as a major factor enabling the transfer of intermediates produced by the n-heptane kernels to leaner mixture fractions (Fig. 14). Finally, the behaviour of the cross scalar dissipation, namely $\chi_c = 2D\boldsymbol{\nabla}\mathrm{Y}_{\mathrm{CH_4}} \cdot \boldsymbol{\nabla}\mathrm{Y}_{\mathrm{O_2}}$ [54] against C (not shown here), revealed predominantly positive values which indicates a premixed combustion mode [54, 55].

4. Conclusions

Autoignition of n-heptane sprays in a methane/air mixture, relevant to pilot ignited natural gas engines, was investigated by DNS in order to provide some fundamental information of this relatively unexplored problem. Two cases were studied that differed in the amount of n-heptane while the temperature, the methane content in the oxidizer stream, and the turbulence intensity were kept the same. It was found that the presence of methane in the oxidizer stream delays n-heptane autoignition compared to its ignition in pure air. The turbulent spray case ignites later than the minimum autoignition time predicted from homogeneous reactor calculations as previously observed for turbulent non-premixed autoignition [27]. The most reactive mixture fraction (ξ_{MR}) concept discussed for n-heptane autoignition [24, 31] is also valid for dual fuel combustion. However, reducing the amount of n-heptane results in quicker disappearance of ξ_{MR} due to mixing. Therefore the autoignition of n-heptane occurs at leaner mixtures that despite the somewhat longer autoignition time, results in better methane oxidation.

During n-heptane autoignition, methane is slowly consumed but its autoignition time under the nominal conditions is one order of magnitude longer than the autoignition time of n-heptane. Consequently, the n-heptane autoignition kernels act as the source of ignition for the premixed methane flame. Essentially, the methane flame is initiated as a result of heating gained by the pressure rise caused by the n-heptane oxidation and heat and mass transfer of radicals and intermediates from the n-heptane ignition kernels. The difference in the amount of n-heptane between the cases investigated yields different contributions of the above-mentioned mechanisms for the premixed methane flame ignition. For sufficiently large amounts of n-heptane, combustion of n-heptane results in increased pressure rise and significant heating due to adiabatic compression accelerating the slow methane oxidation. Nevertheless, intense methane consumption is initiated when radicals and

intermediate species from the already ignited regions reach the oxidizer stream. On the contrary, for small amounts of n-heptane, intermediates reach the oxidizer stream faster due to the very lean mixtures surrounding the n-heptane ignition kernels. Hence the premixed methane oxidation is initiated at intermediate temperatures.

The difference in the amount of n-heptane also induces different statistical behaviour of the premixed flame when investigated in a progress variable space. The progress variable used is associated with methane mass fraction. For large amounts of n-heptane, the premixed methane oxidation follows an autoignition regime whereas for small amounts of n-heptane a behaviour more similar to a canonical premixed flame is observed.

5. Acknowledgements

The computational costs for this work were covered by the EPSRC project ref. no. EP/J021997/1.

Table 1
Spray and turbulence parameters for the DNS cases investigated

Parameter	Case A	Case B
R	0.55	0.16
Droplets configuration	Layer: $x = 0.35-0.65L$	Sphere: $R = 0.185L$
Φ_0	2.08	4.4
τ_{evap} (ms)	0.998	0.965
$\tau_{turb} = \frac{l_t}{u'}$ (ms)	0.6	0.6
Re_t	60	60

Table 2
The minimum autoignition time,τ_{id}, and the most reactive mixture fraction, ξ_{MR}, from homogeneous reactor calculations. See Section 3 for the initial conditions of these simulations. The autoignition time of the methane-air mixture, $\tau_{id,0}$, is also given.

ϕ_{CH_4}	τ_{id} [ms]	ξ_{MR}	$\tau_{id,0}$ [ms]
0	0.790	0.198	-
0.6	0.834	0.210	16.768

6. Figures

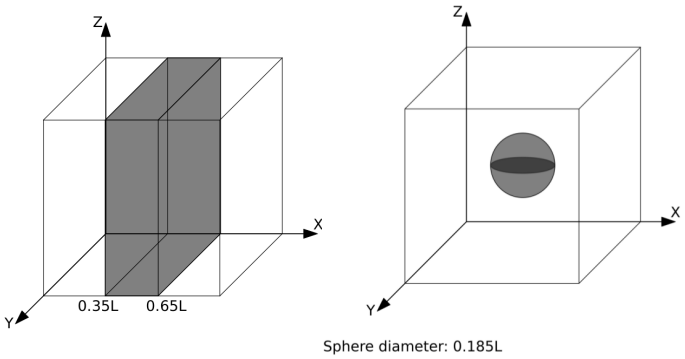

Fig. 1. Schematic of the configuration in case A (left) and case B (right). Grey corresponds to the initial droplet laden regions.

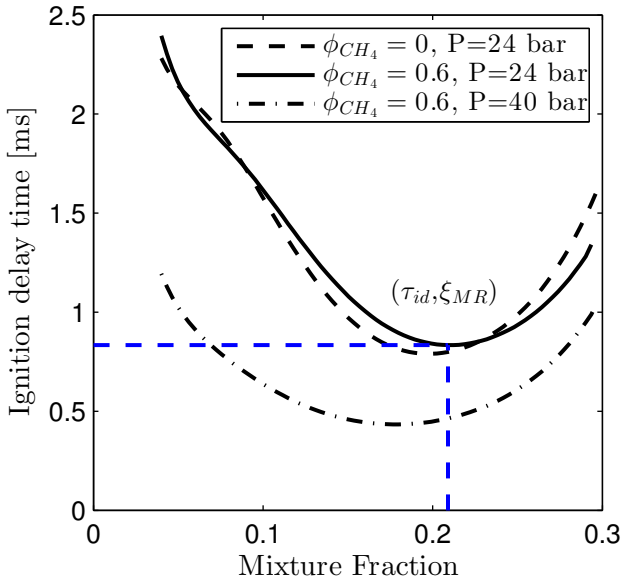

Fig. 2. Ignition delay time of homogeneous n-heptane/oxidizer mixtures, where the oxidizer ($\xi = 0$) is a methane-air mixture at the indicated equivalence ratio (ϕ_{CH_4}) and T_{ox}=1050 K. Each mixture initial condition is determined from inert mixing of the oxidizer and the n-heptane fuel stream ($\xi = 1$, T_F=450 K). For each set of conditions the shortest ignition delay time, namely τ_{id}, is observed for a mixture fraction denoted as ξ_{MR}.

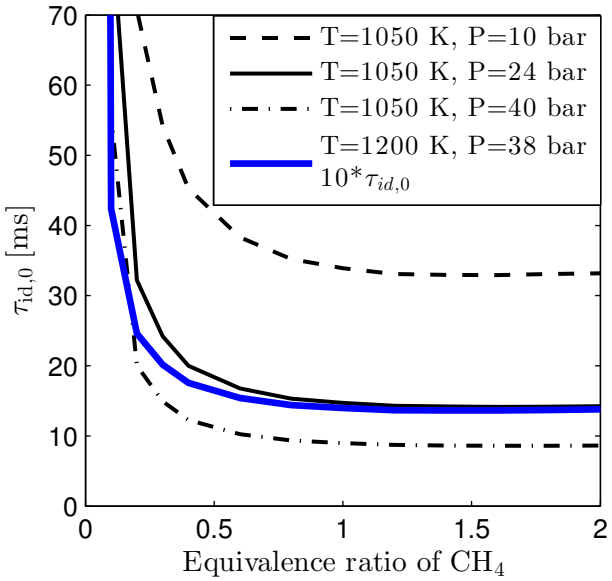

Fig. 3. Ignition delay time of $\xi = 0$ ($\tau_{id,0}$) against ϕ_{CH_4} under different pressures. The value of the $\tau_{id,0}$ is also computed for adiabatic compression conditions from P_0=24 bar (T_0=1050 K) to P_{fin}=38 bar (T_{fin}=1200 K).

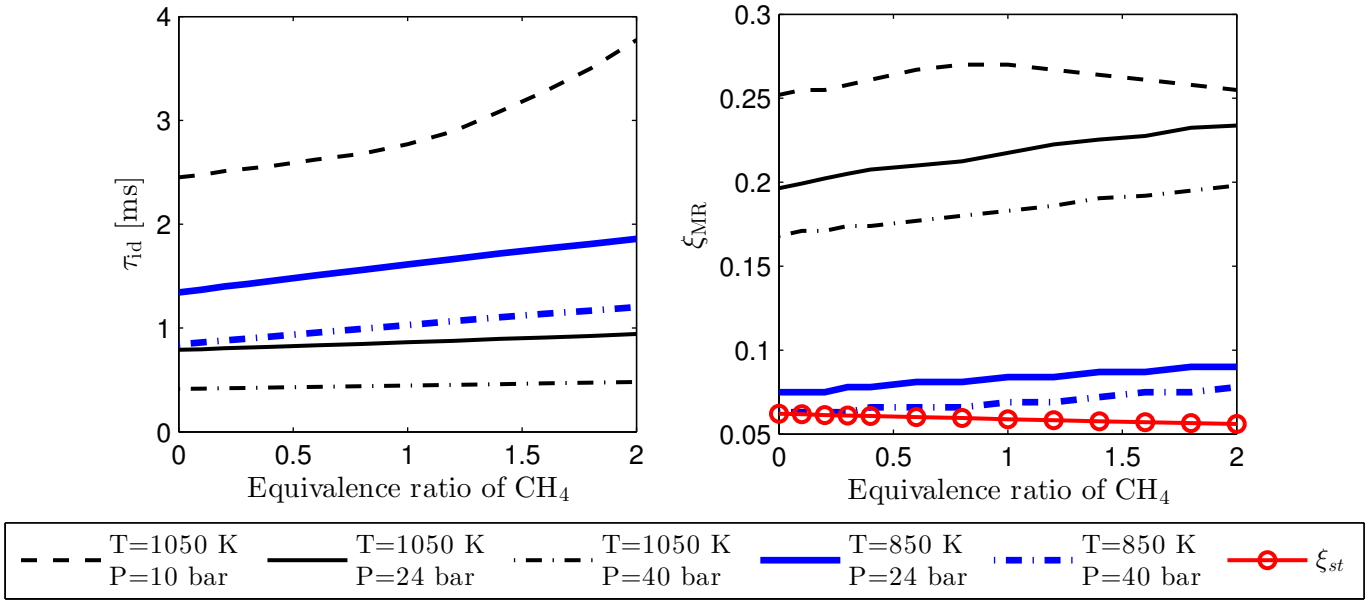

Fig. 4. Left: reference ignition delay time (τ_{id}) of homogeneous n-heptane/oxidizer mixtures for a range of ϕ_{CH_4} in the oxidizer stream. The value of the τ_{id} is computed for different pressures and oxidizer ($\xi = 0$) temperatures while the n-heptane ($\xi = 1$) temperature is 450 K in all cases. Right: most reactive mixture fraction (ξ_{MR}) corresponding to the value of the τ_{id} on the left. The stoichiometric mixture fraction (ξ_{st}) is also shown.

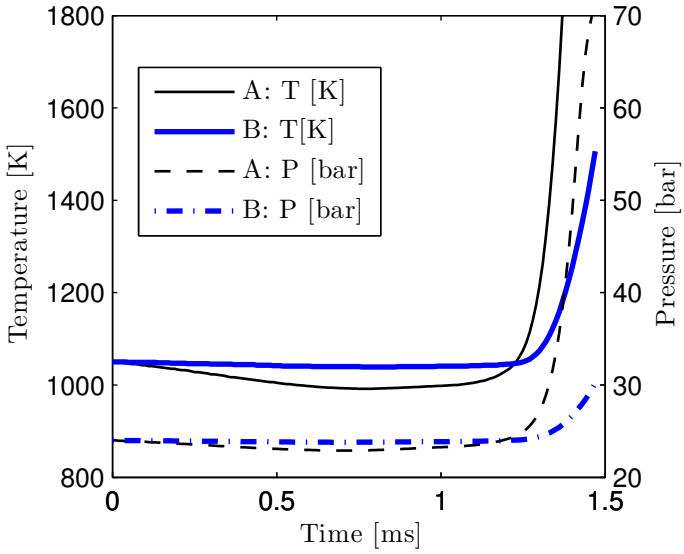

Fig. 5. Temporal evolution of volume averaged temperature and pressure for the DNS cases A and B.

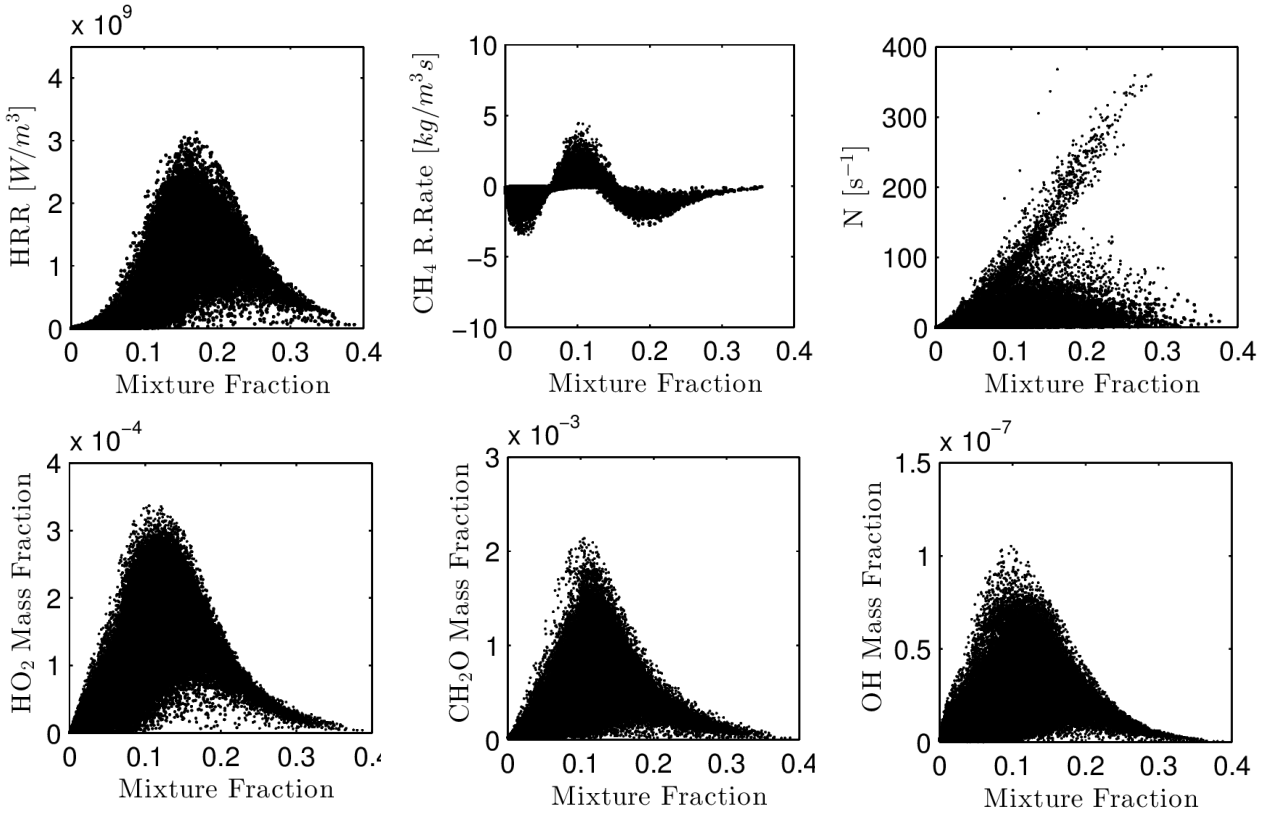

Fig. 6. Scatter plots of heat release rate (HRR), CH_4 reaction rate, scalar dissipation rate (N) and mass fractions of CH_2O, OH and HO_2 at t=0.650 ms. Data shown correspond to case A.

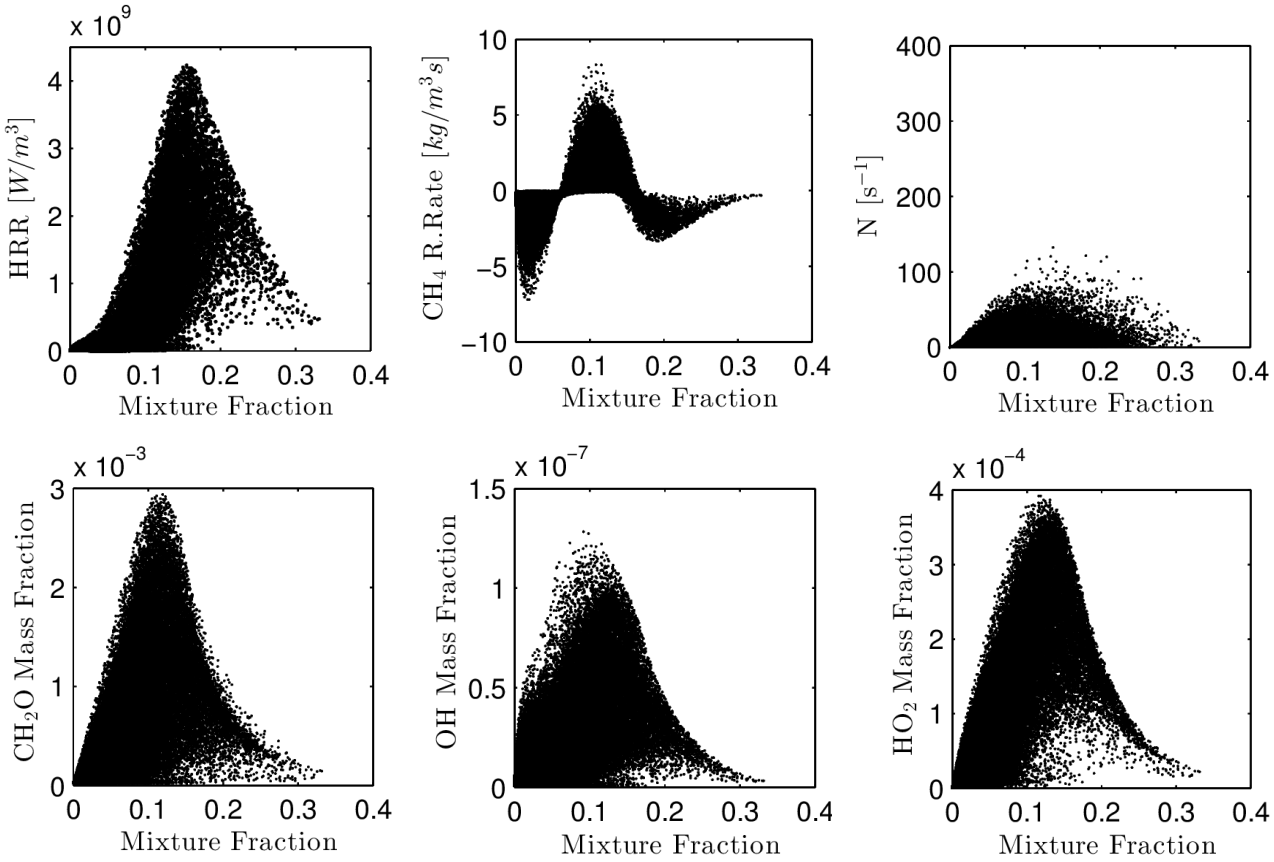

Fig. 7. Scatter plots of heat release rate (HRR), CH_4 reaction rate, scalar dissipation rate (N) and mass fractions of CH_2O, OH and HO_2 at t=0.650 ms. Data shown correspond to case B.

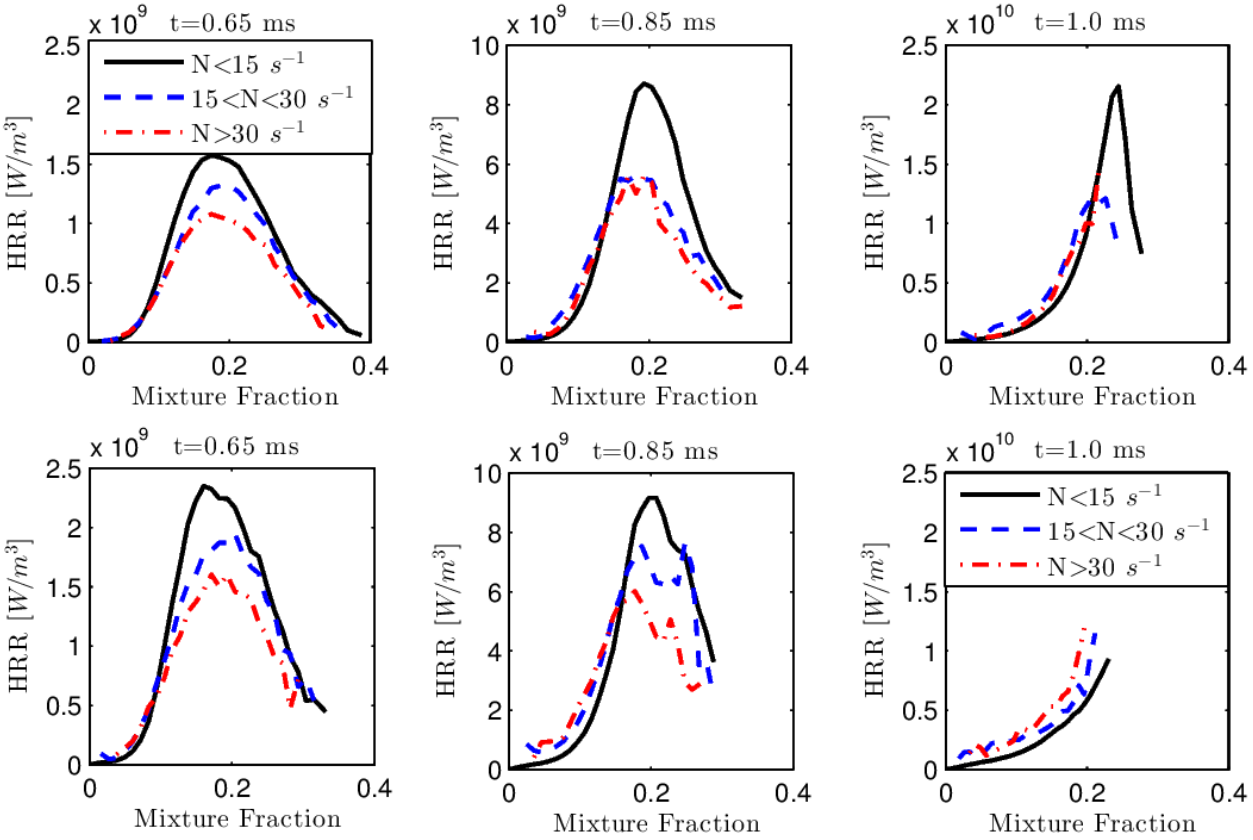

Fig. 8. Doubly conditioned heat release rate (HRR) for the indicated scalar dissipation rate range for case A (upper) and B (lower).

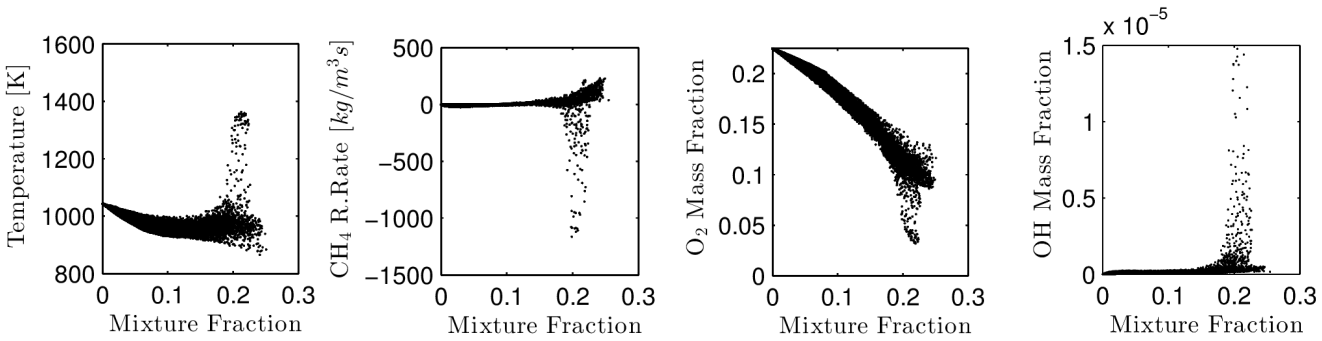

Fig. 9. Scatter plots of temperature, CH_4 reaction rate, and mass fractions of O_2 and OH taken at the ignition time of case A, $\tau_{id}^{DNS,A}$=1.035 ms.

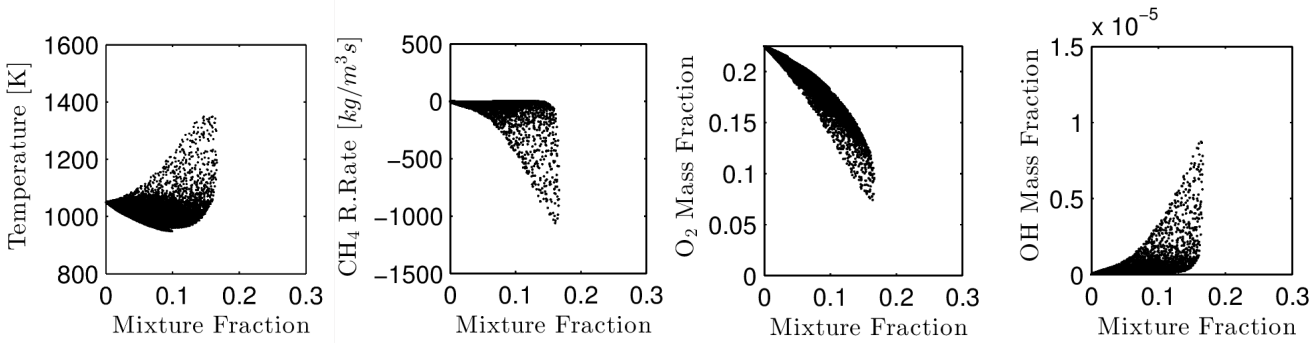

Fig. 10. Scatter plots of temperature, CH_4 reaction rate, and mass fractions of O_2 and OH taken at the ignition time of case B, $\tau_{id}^{DNS,B}$=1.148 ms.

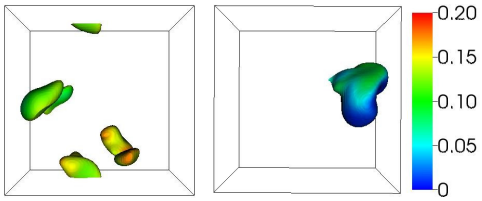

Fig. 11. Iso-surface of T=1250 K coloured by mixture fraction, soon after the first appearance of ignition. Case A (left): t=1.16 ms. Case B (right): t=1.30 ms.

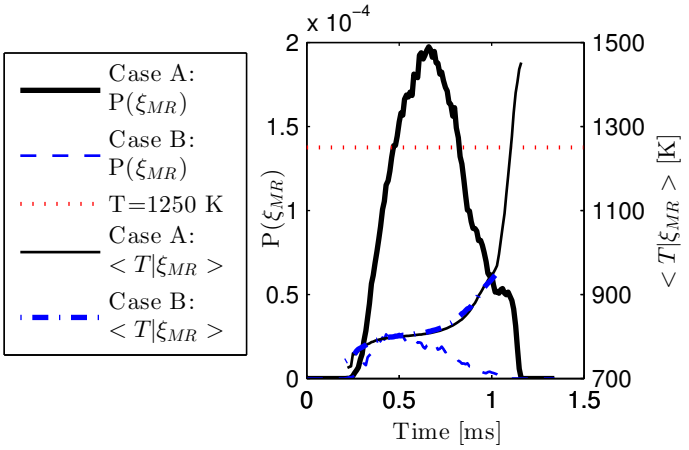

Fig. 12. Temporal evolution of the probability of occurrence of $\xi = \xi_{MR}$ ($P(\xi_{MR})$) and of the corresponding conditional temperature at ξ_{MR} $\langle T|\xi_{MR}\rangle$, with ξ_{MR}=0.21 as predicted by the homogeneous reactor calculations. The threshold of 1250 K used for defining the ignition time is also shown.

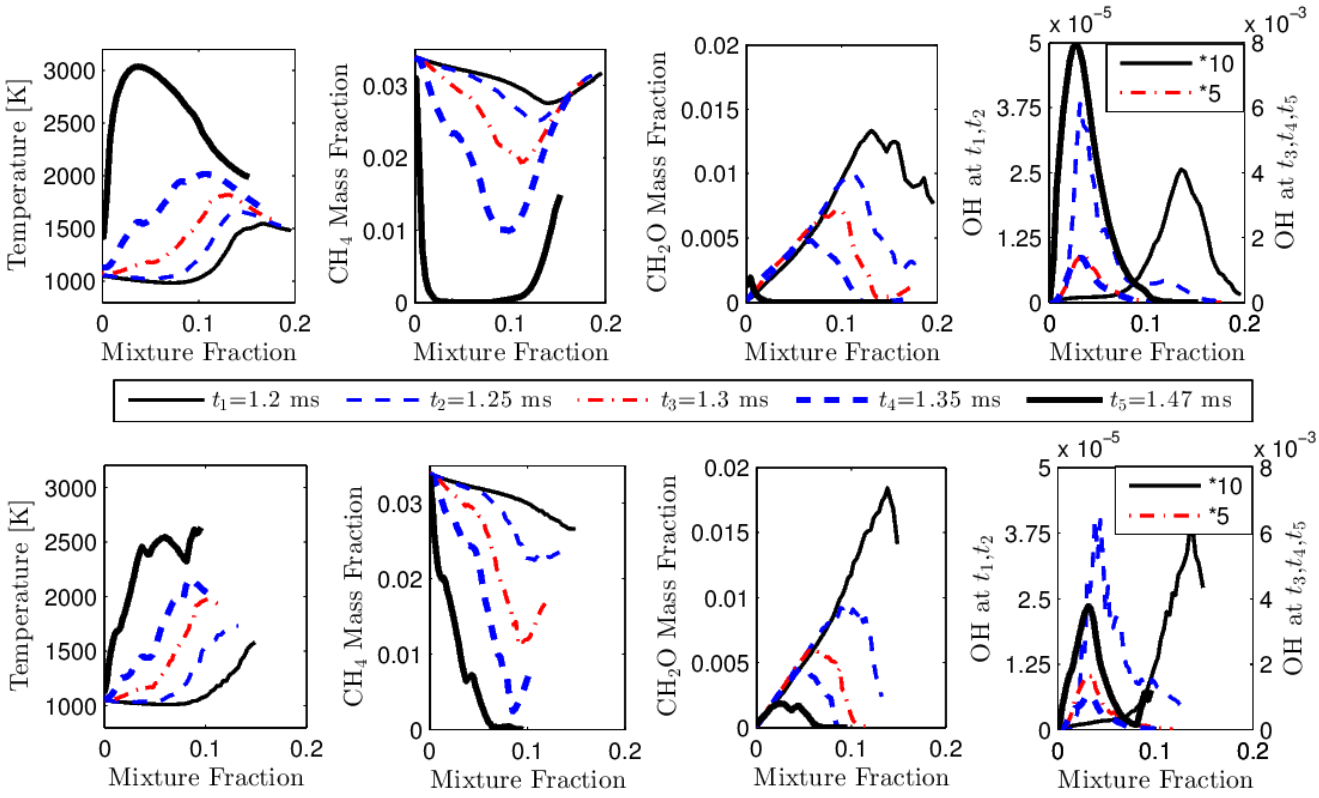

Fig. 13. Conditional averages of temperature, and CH_4, CH_2O, OH mass fractions at the indicated time instants for case A (upper) and B (lower).

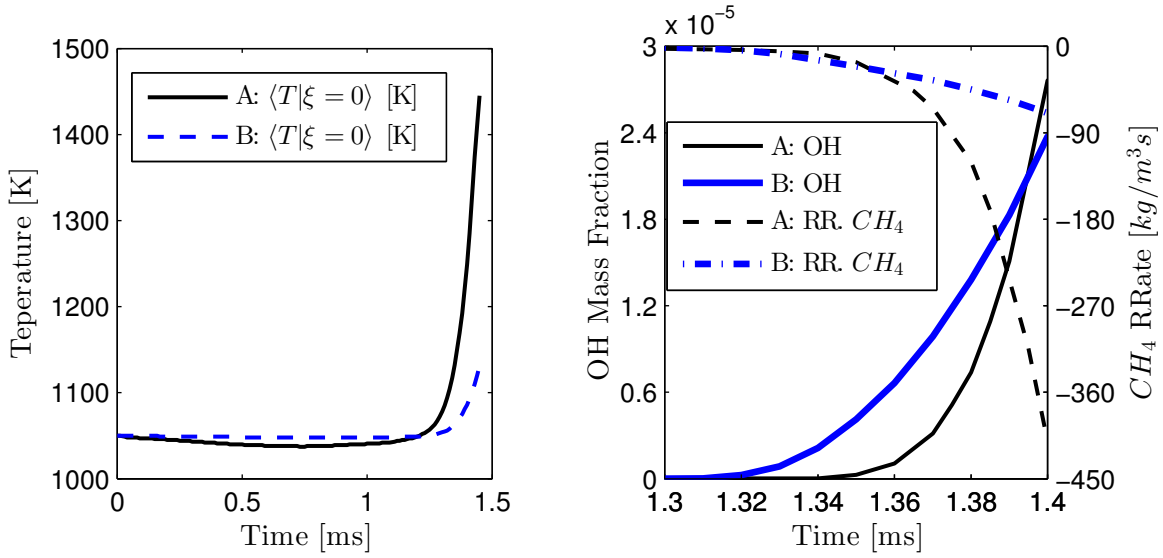

Fig. 14. Temporal evolution of (left) $\langle T|\xi=0\rangle$ and (right) methane reaction rate $\langle RR.CH_4|\xi=0\rangle$ and OH mass fraction $\langle Y_{OH}|\xi=0\rangle$, for both cases, conditional on $\xi=0$.

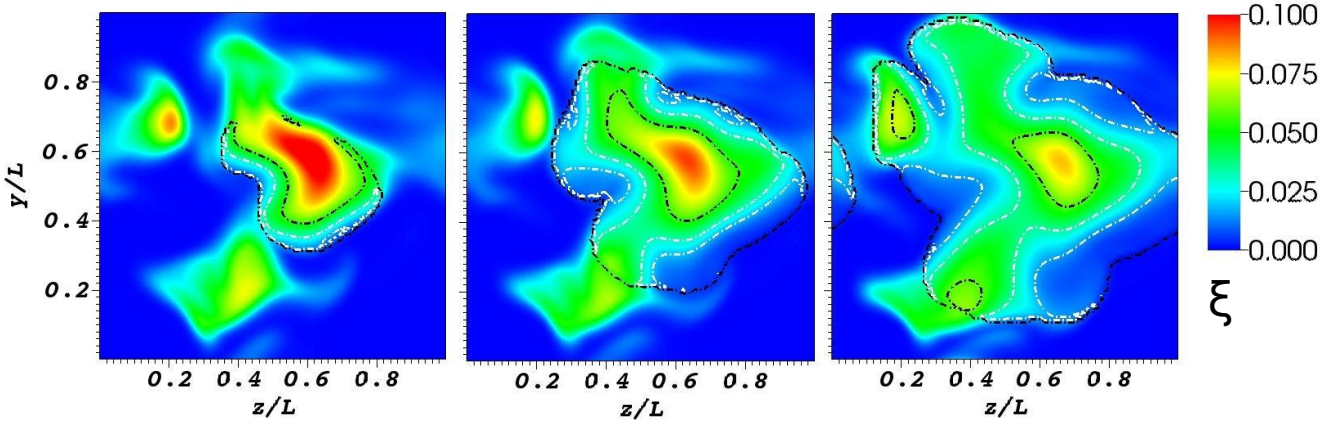

Fig. 15. Shaded contours of ξ and iso-lines of OH mass fraction (8×10^{-4} (black), 5×10^{-3} (white)) taken at x=0.79L, at t=1.32, 1.40, 1.48 ms for case B.

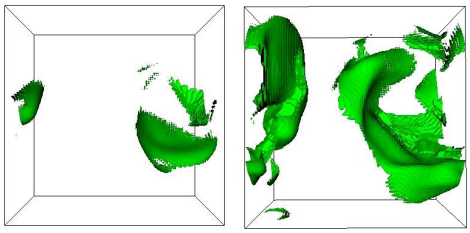

Fig. 16. Iso-surface of C=0.5 at t=1.40 ms (left) and t=1.53 ms (right) for case B.

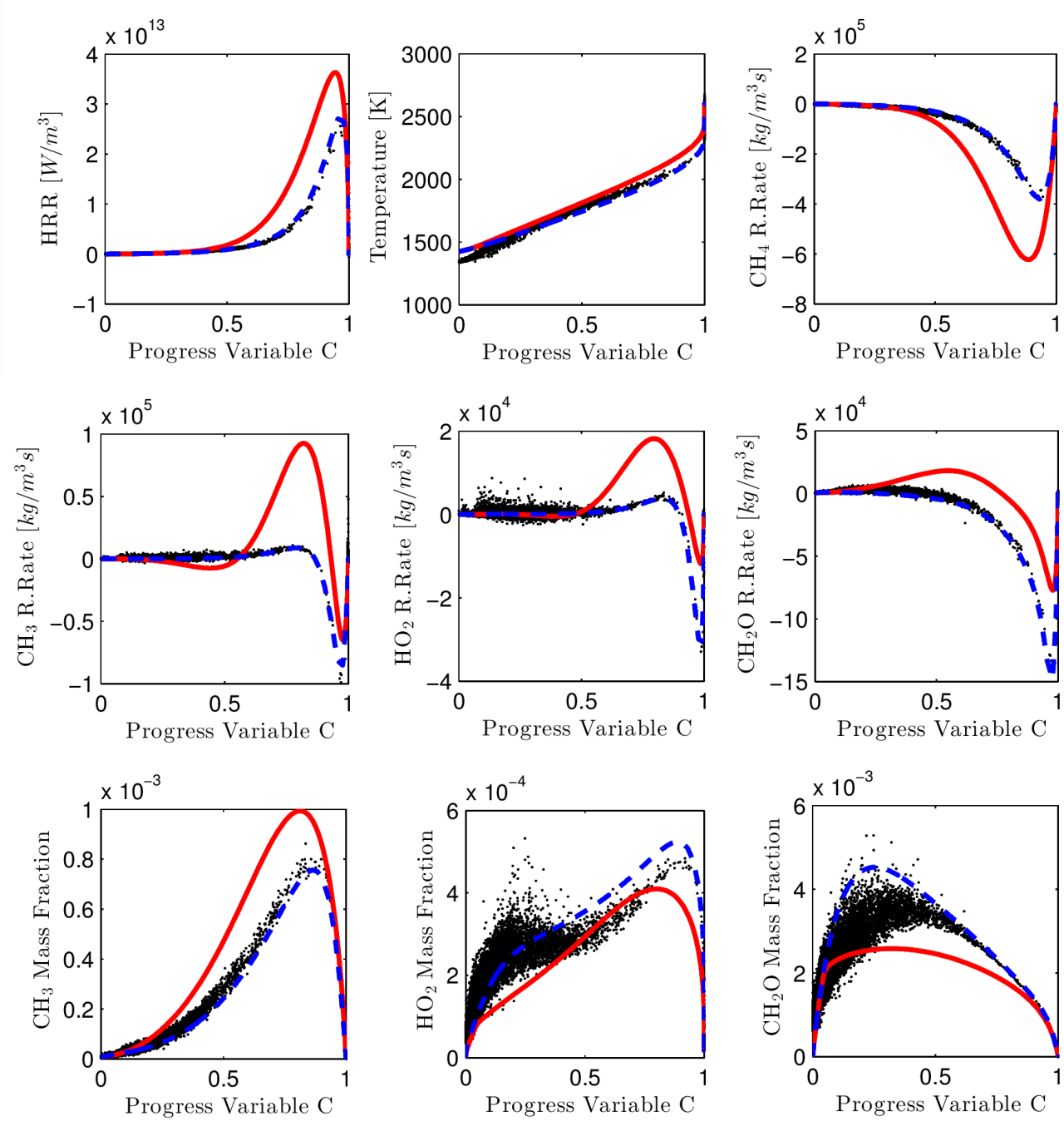

Fig. 17. Scatter plots of heat release rate (HRR), temperature, reaction rates of CH_4, CH_3, HO_2, and CH_2O and mass fractions of CH_3, HO_2, and CH_2O at $\xi = 0$, plotted against the progress variable C and compared with 1-D laminar premixed flame calculations (red continuous line) and homogeneous reactor calculations (blue dashed line). The DNS data (black points) are taken from case A at t=1.47 ms.

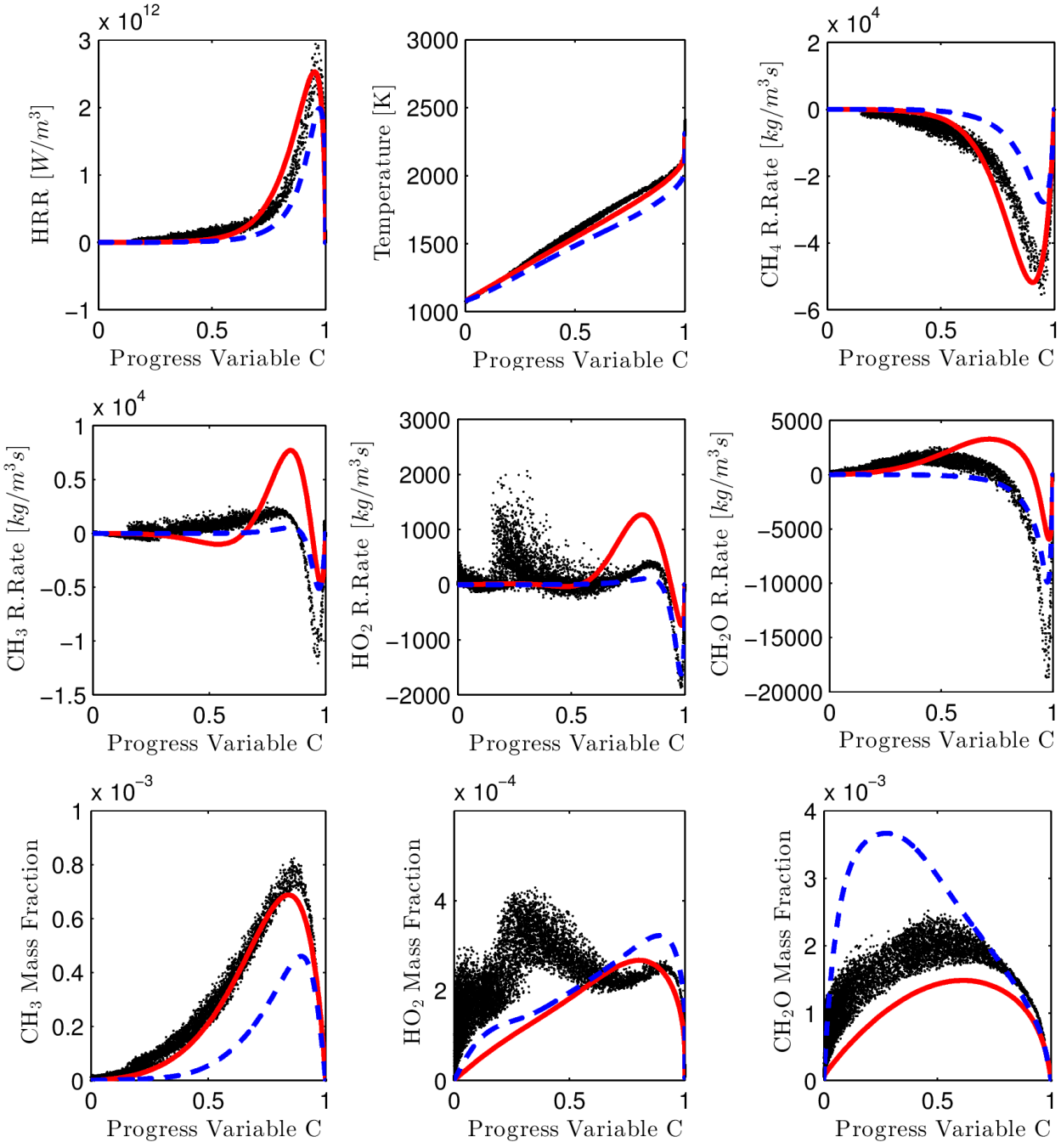

Fig. 18. Scatter plots of heat release rate (HRR), temperature, reaction rates of CH_4, CH_3, HO_2, and CH_2O and mass fractions of CH_3, HO_2, and CH_2O at $\xi = 0$, plotted against the progress variable C and compared with 1-D laminar premixed flame calculations (red continuous line) and homogeneous reactor calculations (blue dashed line). The DNS data (black points) are taken from case B at t=1.4 ms.

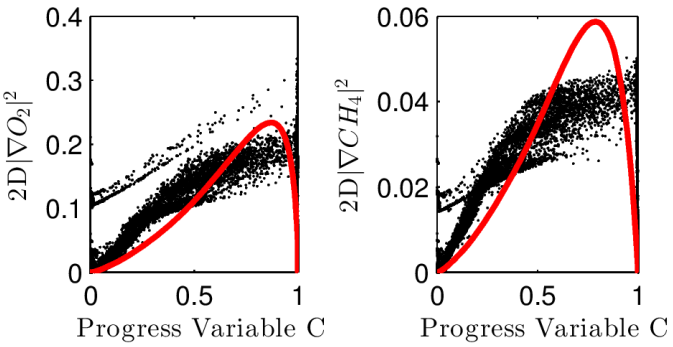

Fig. 19. Scatter plots of dissipation rates of O_2 and CH_4 plotted against the progress variable C and compared with 1-D laminar premixed flame calculations (red continuous line). The DNS data (black points) are taken from case B at t=1.4 ms.

Appendix A. Assessment of the chemical scheme

In this appendix the performance of the reduced chemical scheme employed in the DNS is evaluated by comparing the ignition delay time and most reactive mixture fraction values to the corresponding values resulting from the skeletal scheme from which it was derived [20]. Homogeneous n-heptane/oxidizer mixtures are considered with the oxidizer being a methane/air mixture at various equivalence ratios under the DNS conditions (T_{ox} = 1050 K, T_F = 450 K, P = 24 bar). The Liu et al. (2004) scheme [20] is then examined in the context of methane laminar premixed flame performance by evaluating the laminar flame speed at different conditions as presented earlier in Fig. 4. Following this, the laminar flame speed and species profiles predicted by the Liu et al. (2004) mechanism at the DNS conditions are compared with the corresponding flame speed and species profiles predicted from the GRI-3.0 mechanism [46] that was originally developed for methane. The laminar premixed flame calculations were performed using the Cosilab package [45].

Appendix A.1. Homogeneous reactor calculations

Homogeneous reactor calculations were performed using both the reduced and skeletal mechanism [20] at the nominal conditions (P=24 bar, T=1050 K) in order to examine whether the steady-state approximations used in the reduced scheme affect the retarding effect of methane on n-heptane autoignition. The corresponding ignition delay times and ignition locations in mixture fraction space are illustrated in Fig. A.20 for a range of methane equivalence ratios in the oxidizer stream. The reduced mechanism slightly under-predicts the ignition delay time whereas it slightly overestimates the most reactive mixture fraction. This might be attributed to the steady state assumptions adopted in the reduced scheme. The dominant initiation reaction at low temperatures results in the formation of heptylperoxy radicals (RO_2) which eventually leads to the formation of OH radical through a chain-branching reaction. However, at intermediate temperatures, the addition of O_2 to heptyl radicals shifts towards dissociation back to heptyl and O_2, inhibiting ignition [20]. These reactions are reduced into global steps in the reduced mechanism. Therefore, ignition according to the skeletal mechanism tends to be prolonged. Nevertheless, these differences are small, between 4-5%, leading to the conclusion that the chemical scheme used in the DNS is adequate for the description of the pilot fuel autoignition in the presence of methane.

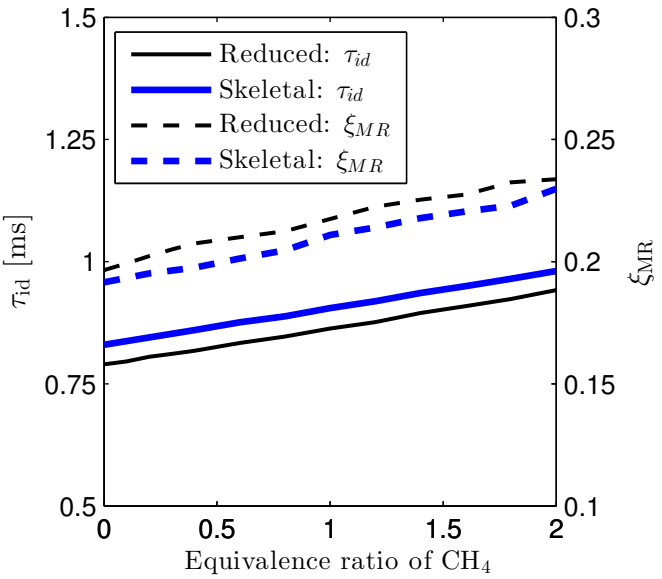

Fig. A.20. Reference ignition delay times (τ_{id}) and most reactive mixture fractions (ξ_{MR}) predicted from the reduced and skeletal scheme. The pressure and temperature of the oxidizer and n-heptane streams are the same as the DNS conditions (P=24 bar, T_{ox}=1050 K, T_F = 450 K).

Appendix A.2. Laminar premixed flame calculations

The n-heptane autoignition will serve as the energy source for the premixed flame initiation [3] and here the chemical mechanism employed is examined in the context of laminar methane premixed flame. Laminar flame speeds were computed at different pressures and temperatures as a function of the equivalence ratio of methane and plotted in Fig. A.21. The conditions investigated are identical with the homogeneous reactor calculations (Fig. 4). Comparison of the flame speeds predicted by the Liu et al. (2004) [20] skeletal scheme with GRI-3.0 [46] is also shown in Fig. A.21 for $T = 850$ K and $T = 1050$ K. It should be noted that the lean flammability limits presented are defined as the equivalence ratio where $S_L/S_{L,0} = 0.1$ with $S_{L,0}$ being the laminar flame speed at stoichiometry. This definition was also adopted by Neophytou et al. (2012) [23] in their investigations on the performance of the chemical mechanism in spark ignition. Precise definition of the lean flammability limits in numerical investigations of methane/air premixed flames, as conducted by Egolfopoulos et al. (2007) [56], are necessary when the conditions considered are close to extinction. Additionally, the lean flammability limits for the premixed methane flame in the presence of the n-heptane vapour may differ from the flammability limits of a pure methane/air mixture [13]. However, since the conditions investigated in this study are far from the lean flammability limit, the above-mentioned criterion [23] was considered adequate for the purpose of assessing the scheme.

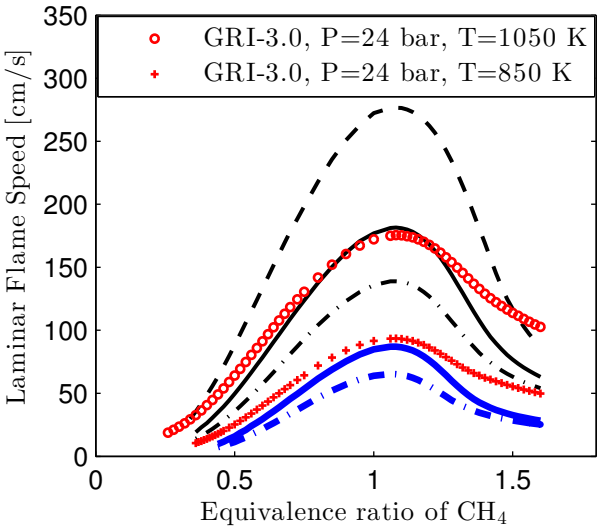

Fig. A.21. Laminar flame speeds computed using the Liu et al. (2004) skeletal scheme [20]. Curves as in Fig. 4.

The laminar flame speed exhibits the expected behaviour: increasing pressure results in reduction of the flame speed. Additionally, higher mixture temperatures exhibit higher flame speeds. Compared to the GRI-3.0 scheme [46], the Liu et al. (2004) [20] scheme predicts reasonably well the laminar flame speeds for a wide range of equivalence ratios ($0.4 \leq \phi_{CH_4} \leq 1.2$) for both temperatures examined and only deviates markedly at the rich limit. Better agreement between the two schemes is accomplished for the high temperature curves ($T = 1050$ K) although for the low temperature ($T = 850$ K) the methane flame speed is also adequately predicted by the Liu et al. (2004) mechanism. Figure A.22 illustrates profiles of CH_4, O_2, CH_2O, OH and temperature. The temperature and species profiles produced with the Liu et al. (2004) [20] scheme are qualitatively and quantitatively close to the profiles produced with the GRI-3.0 scheme. The temperature and species profiles against the flame coordinate in Fig. A.22 give an overall flame thickness of about 0.1 mm, resulting in 5 grid nodes across the flame which is adequate for the purpose of the study presented. Note that for ϕ_{CH_4}=0.6 at the nominal initial conditions (T=1050 K, P=24 bar), S_L= 0.73 m/s and so $u'/S_L = 1.15$ for the resulting turbulent premixed flame of methane while $L_{11}/\delta = 4.4$. Therefore the methane flame would lie in the corrugated flamelet regime according to [51].

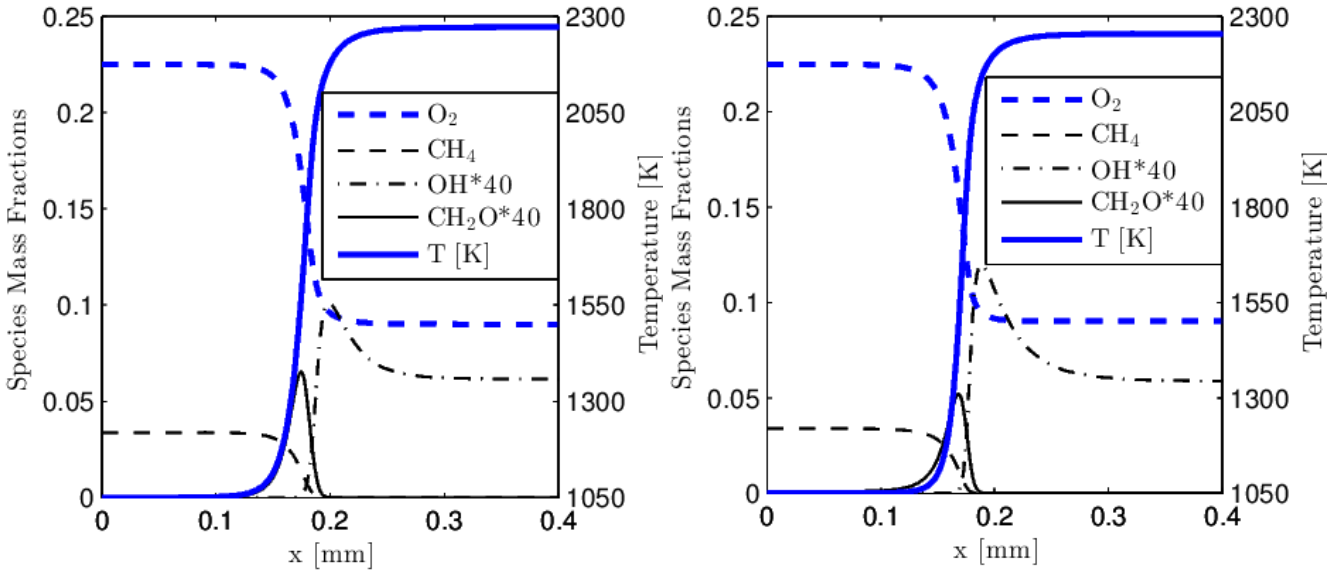

Fig. A.22. Species profiles computed using the GRI-3.0 mechanism [46] (left) and the Liu et al. (2004) [20] skeletal scheme (right) at the nominal conditions; P=24 bar, T=1050 K, $\phi_{CH_4} = 0.6$.

Appendix B. Grid independence

In this appendix the DNS results are explored by comparing the obtained data set with the data set of a supplementary DNS test case with finer grid resolution. In principle, the grid spacing implemented must satisfy two criteria; first it has to be large enough in order for the point source approximation to be valid and secondly it has to be adequately small to resolve the structures present in the simulation. The first condition limits the grid spacing to be of the same order of magnitude with the droplet size so that on the one hand no sub-grid mixing assumptions are being made and on the other hand the Lagrangian particle formulation yields meaningful results [57, 58]. The first condition mainly refers to the stages of evaporation and mixture formation when droplets are present and a detailed description of their evolution is needed. The second condition may constitute a limitation when the premixed flames are dominant and flame statistics are being extracted quite later than the first appearance of premixed flame combustion mode.

The grid spacing initially implemented (23 μm) is adequate to resolve the pre-ignition phase and the early stages of ignition of the n-heptane spray as the profiles are expected to be wide and span over several grid nodes. However, when the premixed methane/air flame is initiated the grid resolution may be questioned as the species profiles are expected to be thin under the employed pressure and temperature conditions. In order to explore the exhibited behaviour (e.g. Fig. 18), the DNS data set was compared to a test-case data set with higher resolution. The test-case actually

represents a restart of the DNS case B at $t = 1.120$ ms onwards after interpolating the solution on a finer grid. The time instant was chosen to be after evaporation was completed and before ignition. The resolution of the finer grid was defined based on the thinnest profile that appears in the laminar premixed flame problem at the conditions when the premixed flame was initiated (P=27 bar, T=1080 K; i.e. the conditions of Fig. 18). The finer grid consists of 300 grid points in each direction resulting in 8 points across the thinnest species profile of the laminar premixed flame (see Fig. B.23). Due to the prohibitive computational cost, results on a finer grid were only performed for case B. Case B is a more stringent test of grid independence because in this case the methane-air mixture combusts in a premixed flame regime.

The profiles of Fig. 18 were repeated using the refined data set (Fig. B.24). The refined profiles are qualitatively and quantitatively similar with the original data set, allowing the description of the flame using the original data. Therefore, the coarse grid implemented on the simulations presented as a restriction resulting from the droplet modelling framework, does not alter the main features of the premixed flame, upholding the conclusions reached with the coarser grid.

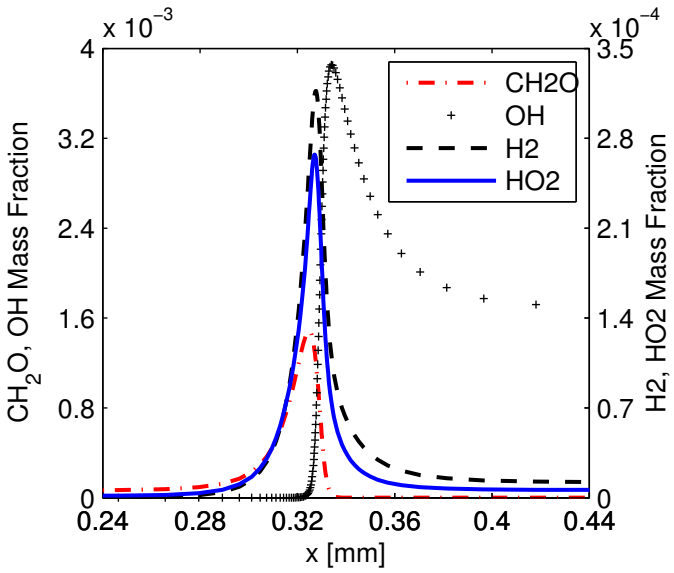

Fig. B.23. Species profiles of a laminar premixed methane/air flame at P=27 bar, T=1080 K, ϕ_{CH_4}=0.6 using the Liu et al. (2004) chemical mechanism [20].

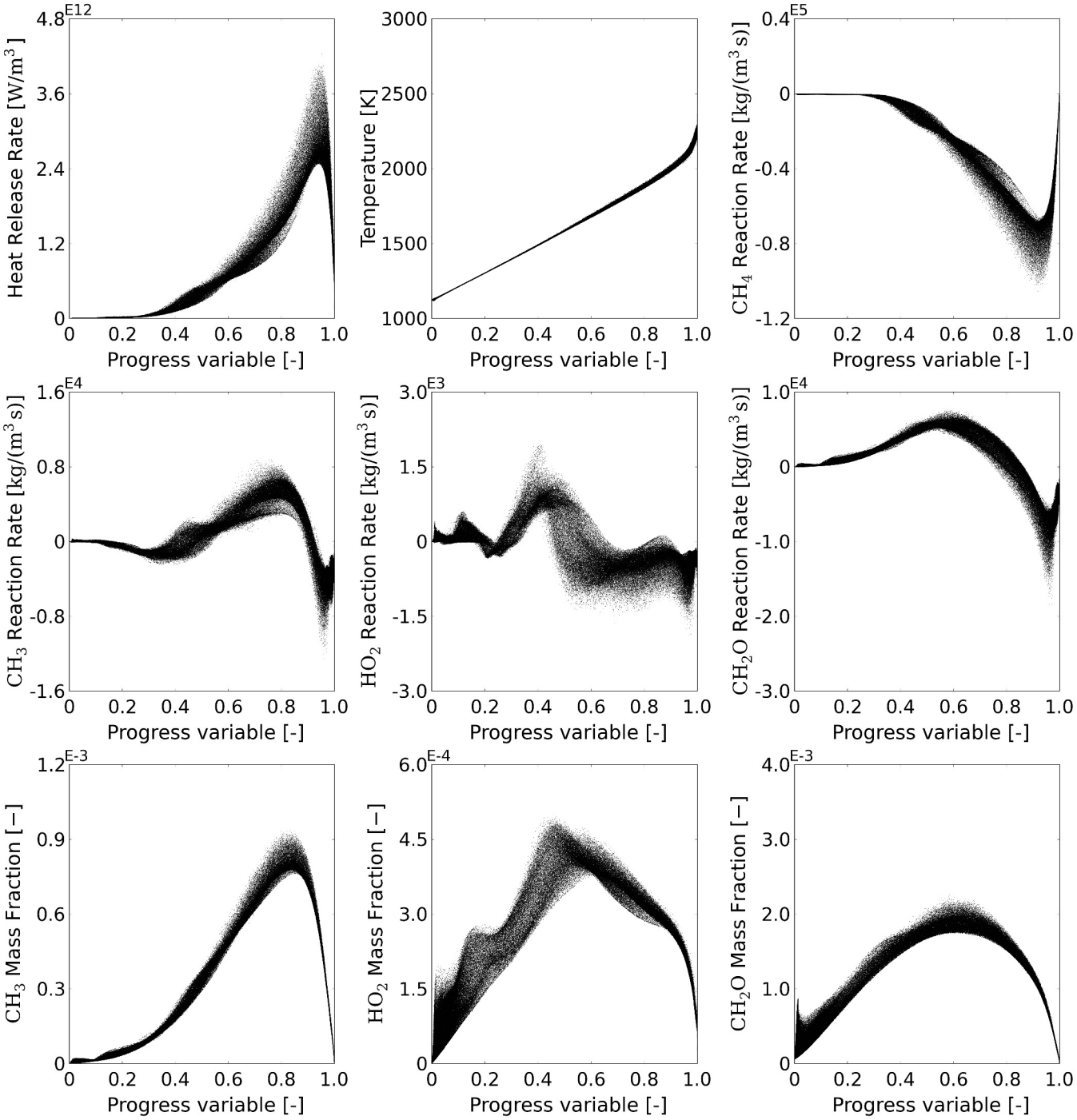

Fig. B.24. Scatter plots of heat release rate (HRR), temperature, reaction rates of CH_4, CH_3, HO_2, and CH_2O and mass fractions of CH_3, HO_2, and CH_2O at $\xi = 0$, plotted against the progress variable C using the test-case data set at t=1.4 ms.

References

[1] R. Reitz, Combust. Flame 160 (2013) 1–8.

[2] R. Papagiannakis, D. Hountalas, Energy Conv. Manag. 45 (2004) 2971–2987.

[3] T. Korakianitis, A. Namasivayam, R. Crookes, Prog. Energy. Combust. Sci. 37 (2011) 89–112.

[4] X. Han, M. Zheng, J. Wang, Fuel 109 (2013) 336–349.

[5] A. Amjad, R. K. Saray, S. Mahmoudi, A. Rahimi, Energy 36 (2011) 6900–6909.

[6] K. K. Srinivasan, S. R. Krishnan, Y. Qi, K. C. Midkiff, H. Yang, Combust. Sci. Technol. 179 (2007) 1737–1776.

[7] W. P. Attard, E. Toulson, A. Huisjen, X. Chen, G. Zhu, H. Schock, SAE Paper 2012-01-0823 (2012).

[8] S. Kammerstätter, S. Bauer, T. Sattelmayer, SAE Paper ICEF2012-92031 (2012).

[9] E. Khalil, P. Samuel, G. A. Karim, SAE Paper 961932 (1996).

[10] G. A. Karim, Prog. Energy Combust. Sci. 6 (1980) 277–285.

[11] S. Schlatter, B. Schneider, Y. M. Wright, K. Boulouchos, SAE Paper 010825 (2012).

[12] N. Iida, M. Nakamura, H. Ohashi, SAE Paper 970899 (1997).

[13] O. Badr, G. A. Karim, B. Liu, Appl. Therm. Engin. 19 (1999) 1071–1080.

[14] C. S. Lee, K. H. Lee, D. S. Kim, Fuel 82 (2003) 553–560.

[15] M. Mbarawa, B. E. Milton, R. T. Casey, Int. J. Therm. Sci. 40 (2001) 927–936.

[16] S. Schlatter, B. Schneider, Y. M. Wright, K. Boulouchos, 3D-CRFD Combustion modeling of gas engines with pilot injection, Proc. 7th Dessau Gas Engines Conf., 2011.

[17] A. Maghbouli, R. Saray, S. Shafee, J. Ghafouri, Fuel 106 (2013) 98–105.

[18] S. Amzin, N. Swaminathan, J. W. Rogerson, J. H. Kent, Combust. Sci. Technol. 184 (2012) 1743–1767.

[19] S. Amzin, N. Swaminathan, Combust. Theory Model. 17 (2013) 1125–1153.

[20] S. Liu, J. C. Hewson, J. H. Chen, H. Pitsch, Combust. Flame 137 (2004) 320–339.

[21] A. Neophytou, E. Mastorakos, R. S. Cant, Combust. Flame 157 (2010) 1071–1086.

[22] A. Neophytou, E. Mastorakos, R. S. Cant, Proc. Combust. Inst. 33 (2011) 2135–2142.

[23] A. Neophytou, E. Mastorakos, R. S. Cant, Combust. Flame 159 (2012) 641–664.

[24] G. Borghesi, E. Mastorakos, R. S. Cant, Combust. Flame 160 (2013) 1254–1275.

[25] P. Schroll, A. P. Wandel, R. S. Cant, E. Mastorakos, Proc. Combust. Inst. 32 (2009) 2275–2282.

[26] A. P. Wandel, Proc. Combust. Inst. 34 (2013) 1625–1632.

[27] E. Mastorakos, Prog. Energy Combust. Sci. 35 (2009) 57–97.

[28] M. Klein, N. Chakraborty, R. S. Cant, Flow Turbul. Combust. 81 (2008) 583–607.

[29] N. Chakraborty, M. Klein, Proc. Combust. Inst. 32 (2009) 1435–1443.

[30] K. Nakabe, Y. Mizutani, Combust. Flame (1991) 3–14.

[31] G. Borghesi, Autoignition in turbulent two-phase flows, Ph.D. thesis, Unversity of Cambridge, United Kingdom, 2012.

[32] D. Frank-Kamenetskii, Diffusion and Heat Transfer in Chemical Kinetics, 2nd ed., Plenum Press, New York, 1969.

[33] M. C. Yuen, L. W. Chen., Combust. Sci. Technol. 14 (1976) 147–154.

[34] B. Abramzon, W. A. Sirignano, Int. J. Heat Mass Transfer 32 (1989) 1605–1618.

[35] K. W. Jenkins, R. S. Cant, in: Proc. 2nd AFOSR Conf. DNS LES, Kluwer Academic Publishers, 1999.

[36] T. Dunstan, K. Jenkins, Int. J. Hydrogen Energy 34 (2009) 8389–8404.

[37] C. Kennedy, M. Carpenter, Appl. Numer. Math. 14 (1994) 397–433.

[38] H. N. Najm, P. S. Wyckoff, O. M. Knio, J. Comput. Phys. 143 (1998) 381–402.

[39] O. M. Knio, H. N. Najm, P. S. Wyckoffy, J. Comput. Phys. 154 (1999) 428–467.

[40] C. Kennedy, M. Carpenter, R. Lewis, Appl. Numer. Math. 35 (2000) 177–219.

[41] P. Brown, G. Byrne, A. Hindmarsh, J. Sci. Stat. Comput. 10 (1989) 1038–1051.

[42] H. Ciezky, G. Adomeit, Combust. Flame 93 (1993) 421–433.

[43] Y. M. Wright, O. Margari, K. Boulouchos, G. De-Paola, E. Mastorakos, Flow Turbul. Combust. 84 (2010) 49–78.

[44] G. Borghesi, E. Mastorakos, C. Devaud, R. Bilger, Combust. Theory Model. 15 (2011) 725–752.

[45] Rotexo-Softpredict-Cosilab, GmbH and Co. KG Bad Zwischenahn (Germany), Cosilab Collection, Version 3.0, www.SoftPredict.com, 2009.

[46] G. P. Smith, D. M. Golden, M. Frenklach, N. W. Moriarty, B. Eiteneer, M. Goldenberg, C. T. Bowman, R. K. Hanson, S. Song, W. C. J. Gardiner, V. Lissianski, Z. Quin (2000). URL: `http://www.me.berkeley.edu/gri_mech/`.

[47] K. Harstad, J. Bellan, Int. J. Multiphase Flow 26 (2000) 1675–1706.

[48] G. Batchelor, A. Townsend, Proc. R. Soc. Lond. Ser. A 194 (1948) 527–543.

[49] S. Turns, An Introduction to Combustion, McGraw Hill, 2000, p. 701.

[50] E. Mastorakos, T. A. Baritaud, T. J. Poinsot, Combust. Flame 109 (1997) 1998–223.

[51] N. Peters, Turbulent combustion, Cambridge University Press, 2000.

[52] I. Glassman, R. A. Yetter, Combustion, 4^{th} ed., Elsevier, 2008, p. 114.

[53] T. Echekki, E. Mastorakos, Turbulent Combustion Modeling, Springer, 2011,p. 101.

[54] V. Favier, L. Vervisch, Combust. Flame 125 (2001) 788–803.

[55] N. Chakraborty, E. Mastorakos, Flow Turbul. Combust. 80 (2008) 155–186.

[56] F. N. Egolfopoulos, A. T. Holley, C. K. Law, Proc. Combust. Inst. 31 (2007) 3015–3022.

[57] C. T. Crowe, D. E. Stock, M. P. Sharma, J. Fluis Eng. 99 (1977) 325–332.

[58] Y. Wang, C. J. Rutland, Combust. Flame 149 (2007) 353–365.

List of figure captions